A Structural Investigation of the Passive Film on Iron and Iron/Chromium Alloys

by

Mouass KERKAR

Ingénieur d'État, Master of Science

A thesis submitted to the University of Warwick for admission to the degree of Doctor of Philosophy

Department of Physics

University of Warwick

Coventry CV4 7AL

U.K.

December 1989

To the memory of my parents

Contents

	page
Figure Captions	ix
List of Tables	xii
Acknowledgements	xiii
Declaration	xiv
Abstract	xv
Chapter 1	
General Introduction	1
1.1 Iron and its Alloys in Engineering	1
1.2 General Corrosion	2
1.2.1 Electrochemical Nature of the Corrosion	2
1.2.2 Pourbaix Diagrams	4
1.2.3 Protection against Corrosion	4
1.3 Structural Investigations of the Passive Film on Fe and Fe/Cr Alloys by Using Ex-situ and In-situ Techniques	8
1.3.1 Ex-situ Investigations	9
1.3.2 In-situ Investigations	11
1.3.3 Summary	14
1.4 The Aim of the Work Reported in this Thesis	15
1.5 Plan of the Thesis	16

Chapter 2

Techniques Used for Studying Passivated Films of Fe and Fe/Cr Alloys 17

2.1 Introduction 17

2.2 Photocurrent Spectroscopy 17

2.2.1 Introduction 17

2.2.2 Theory of Photocurrent Spectroscopy 20

2.2.2.1 Wave Length Dependence of the Photocurrent 21

2.2.2.2 Potential Dependence of the Photocurrent 21

2.3 Extended X-ray Absorption Fine Structure (EXAFS) 22

2.3.1 Introduction 22

2.3.2 Theory of EXAFS 23

2.3.3 Extraction of Structural Information from EXAFS 27

2.3.4 The Phase Shift Determination 29

2.3.5 General Methods of Measuring EXAFS 29

2.3.5.1 Transmission EXAFS 30

2.3.5.2 Fluorescence EXAFS 30

2.3.5.3 Electron Yield EXAFS 33

Chapter 3

Experimental 35

3.1 Introduction 35

3.2 Photocurrent Spectroscopy Experiment 35

3.2.1 Introduction 35

3.2.2 Signal Detection 35

3.2.3 The Experimental Apparatus 38

3.2.3.1 The Optical System 38

3.2.3.2 The Electrochemical Control Equipment 41

3.2.3.3 Data Acquisition of the Photocurrent 41

3.2.3.4 The Electrochemical Cells and Electrodes 42

3.2.4 Preparation of the Solutions and Glassware 45

3.2.5 Electrode Preparation 45

3.2.6 Experimental Procedure 46

3.2.6.1 Polarisation Measurements 46

3.2.6.2 Photocurrent Measurements 46

a. Wave Length Dependence of the Photocurrent 46

b. Potential Dependence of the Photocurrent 48

3.3 X-ray Absorption Spectroscopy Experiment 49

3.3.1 Introduction 49

3.3.2 The Experimental Apparatus 49

3.3.2.1 The Optical System 49

3.3.2.2 The Fluorescence EXAFS Detection 51

3.3.2.3 The Fluorescence EXAFS Data Collection 52

3.3.2.4 The Electrochemical Cell and Samples 54

3.3.3 The Sample Preparation 57

3.3.4 Experimental Procedure 59

3.3.4.1 Fluorescence EXAFS Measurements 59

3.3.4.2 Transmission EXAFS Measurements 60

Chapter 4

Electrochemical and Photoelectrochemical Behaviour of Iron and Iron/Chromium Alloys 61

4.1 Introduction 61

4.2 Results and Discussion of the Electrochemical and Photoelectrochemical Studies of Bulk Iron and Iron/Chromium Alloys 61

4.2.1 Electrochemical Behaviour 61

4.2.2 The Energy Dependance of the Photocurrent Spectroscopy Data 63

4.2.3 The Potential Dependence of the Photocurrent Data 69

4.3 Results and Discussion of the Iron and Iron/Chromium Alloys Prepared as Films 71

4.3.1 Electrochemical Behaviour 71

4.3.2 The Energy Dependence of the Photocurrent 71

4.3.3 The Potential Dependence of the Photocurrent 75

4.4 Summary 79

Chapter 5

X-ray Absorption Spectroscopy Results and Discussion 81

5.1 Introduction 81

5.2 Model Compounds 81

5.2.1 Iron Oxide Model Compounds 81

5.2.2 Chromium Oxide Model Compound 82

5.3 Error Analysis 86

5.4 The In-situ and Ex-situ EXAFS Results of the Passive Film Formed on Pure Fe and Fe/Cr Alloys by Simple Immersion in Solution 88

5.4.1 Introduction 88

5.4.2 Results and Discussion of Fe and Fe/Cr Alloy Films at Fe K-Absorption Edge 88

5.4.2.1 Wet Films Formed in 0.1 M $NaNO_2$ 88

5.4.2.2 Dry Films Formed in 0.1 M $NaNO_2$ 90

5.4.2.3 Wet Films Formed in 0.005 M K_2CrO_4 92

5.4.3 Ex-situ and In-situ EXAFS Results at Cr K-Absorption Edge and their Discussion 95

5.4.3.1 Samples Passivated in 0.005 M K_2CrO_4 95

a. Bulk and Film of Pure Fe 95

b. Fe15%Cr and Fe25%Cr Alloys 99

5.4.3.2 Fe25%Cr Alloy Passivated in 0.1 M $NaNO_2$ 99

5.5 The Electrochemical Passivation Results and Discussion 103

5.5.1 Electrochemical Behaviour 103

5.5.2 Fe and Fe25%Cr Samples Passivated in Borate Buffer Solution (pH 8.4) 103

5.5.3 Fe and Fe25%Cr Samples Passivated in Sodium Perchlorate Solution 107

5.5.4 γ-FeOOH Films Electrodeposited from Fe^{2+} Containing Borate Buffer and Ammonium Sulphate Solutions 111

5.6 Discussion of the Structure of the Passive Film on Fe and Fe/Cr Alloys 111

5.6.1 Fe K-Absorption Edge 111

5.6.1.1 Film Formed on Iron 111

5.6.1.2 Film Formed on Fe/Cr Alloys 115

5.6.2 Cr K-Absorption Edge 115

Chapter 6

Conclusions and Suggestions for Further Work 118

References 124

Figure Captions

1.1. A schematic illustration of typical electrochemical corrosion without applied e.m.f. 3

1.2. A schematic representation of a cathodic protection. 3

1.3. A simplified Pourbaix diagram for iron[1]. 5

1.4. A schematic representation of corrosion protection with a sacrificial anode. 7

2.1. A schematic diagram of illuminated p-type and n-type passive films under depletion conditions. The photoelectrochemical reaction for an n-type film is also illustrated. 19

2.2. An X-ray absorption spectrum showing the three different regions. 24

2.3. Modulation of the absorption cross-section leading to EXAFS. The solid lines represent the outgoing photoelectron wave, whereas the dashed lines represent the back-scattered wave. 26

2.4. A schematic diagram of transmission of an X-ray beam through a sample of a given thickness x. 31

2.5. A schematic diagram of the experimental arrangement for recording the transmission EXAFS. 31

2.6. A schematic diagram of (a) fluorescence and (b) Auger emissions when an excited state relaxes. 32

3.1. A simplified block diagram of a pad (Brookdeal 9503). 37

3.2. A schematic representation of an experimental set up for photoelectrochemical studies of passive films. 39

3.3. A schematic representation of the cell used for the polarisation experiments. 43

3.4. The electrochemical cell used for the photoelectrochemical experiments. 44

3.5. A schematic representation of the experimental configuration for recording an EXAFS spectrum. 50

3.6. A schematic diagram of the front of the fluorescence detection unit used in this work. The circles represent the individual Ge solid state detectors. 53

3.7. A cell used in the *in-situ* EXAFS experiments to study films passivated both electrochemically and by immersion into the solution. 55

3.8. An alternative electrochemical cell used here in the *in-situ* EXAFS studies of the passive film. 56

4.1. Polarisation curves in borate buffer solution for bulk Fe and various Fe/Cr alloys. 62

4.2. Energy dependence of the photocurrent spectra, normalised to the lamp emission, for the bulk samples passivated at + 0.9 V in borate buffer solution. 64

4.3. $((i_{ph}/I_l).h\nu)^{1/2}$ vs. $h\nu$ plots for the bulk samples passivated at + 0.9 V in borate buffer. 65

4.4. $((i_{ph}/I_l).h\nu)^{1/2}$ vs. $h\nu$ plots for bulk Fe18%Cr alloy passivated at different potentials in borate buffer solution. 68

4.5. Potential dependence of the photocurrent spectra for the bulk samples passivated at + 0.9 V in borate buffer solution. 70

4.6. Potential dependence of the photocurrent spectra for the bulk samples passivated at + 0.9 V in sodium hydroxide solution (pH 13). 72

4.7. Polarisation curves in borate buffer solution for 100 λ thick films of Fe and various Fe/Cr alloys evaporated onto mylar substrate. 73

4.8. Energy dependence of the photocurrent spectra, normalised to the lamp emission, for film samples passivated at + 0.9 V in borate buffer solution. 74

4.9. $((i_{ph}/I_l).h\nu)^{1/2}$ vs. $h\nu$ plots for the film samples passivated at + 0.9 V in borate buffer solution. 76

4.10. Potential dependence of the photocurrent spectra for 100 λ thick films of Fe and various Fe/Cr alloys passivated at + 0.9 V in borate buffer. These films were also deposited directly onto mylar substrate. 78

5.1. k^3 weighted EXAFS spectrum above Fe K-absorption edge for $\alpha-Fe_2O_3$ model compound and the best fit theoretical curve. The corresponding Fourier transforms are also shown. 84

5.2. k^3 weighted EXAFS spectrum above Cr K-absorption edge for $\alpha-Cr_2O_3$ model compound and the best fit theoretical curve. 87

5.3. k^3 weighted EXAFS spectrum above Fe K-edge for Fe8%Cr passivated by immersion in 0.1 M $NaNO_3$. (a) and (b) show the raw and filtered data respectively with the best fit theoretical curves as well as the corresponding Fourier transforms. 91

5.4. Ex-situ X-ray absorption spectra at Cr K-edge, using the fluorescence mode, for (a) Fe, (b) Fe15%Cr and (c) Fe25%Cr dipped in 0.005 M K_2CrO_4. 94

5.5. EXAFS spectrum above Cr K-edge and its Fourier transform for an Fe foil dipped in 0.005 M K_2CrO_4 solution. The dashed lines represent the fit theoretical curves. 96

5.6. EXAFS spectrum above Cr K-edge and Fourier transform for commercial $Cr(OH)_3$ compound. The best fit theoretical curves are also shown. 98

5.7. Experimental and theoretical EXAFS spectra above Cr K-edge and the corresponding Fourier transforms for an Fe25%Cr alloy passivated in 0.1 M $NaNO_2$ solution. 101

5.8. Polarisation curves in borate buffer solution for a 100 Å thick film of Fe on mylar, a 200 Å thick film of Au on mylar and a 20 Å thick film on gold on mylar. 104

5.9. Polarisation curves in sodium perchlorate for bulk iron, 100 Å thick film of iron and 20 Å thick film of iron evaporated on gold. 105

5.10. X-ray absorption spectra in the region of the Fe K-edge for (a) a 20 Å Fe film at −0.7 V in borate buffer and (b) the same film at + 0.8 V. 108

5.11. k^3 weighted EXAFS spectra for Fe film at + 0.8 V in sodium perchlorate and the corresponding Fourier transforms. 109

5.12. k^3 weighted theoretical EXAFS spectra for Fe film at + 0.8 V in perchlorate. S_1 and S_2 represent the theoretical first and second shells contribution respectively. 110

5.13. XANES spectra at Fe K-edge for, (a) a 20 Å Fe film at + 0.8 V in perchlorate solution, (b) γ−FeOOH and (c) γ−Fe_2O_3. 112

5.14. Atomic radial distribution functions calculated from EXAFS analyses for an Fe film at + 0.8 V in perchlorate solution and for various model compounds. 114

5.15. XANES spectra at Cr K-edge for (a) an Fe foil dipped in K_2CrO_4 solution, (b) $Cr(OH)_3$, (c) Cr_2O_3 and (d) K_2CrO_4. 116

6.1. A representation of the structure of the passive film and the basic building unit, trimers of $[FeO_6]$ octahedra[31]. 119

List of Tables

4.1. Apparent optical band gaps of bulk iron and iron/chromium alloys passivated in borate buffer solution at various voltages. 67

4.2. Flat band potentials of bulk iron and iron/chromium alloys passivated at + 0.9 V in borate buffer (pH 8.4) and 0.1 M NaOH (pH 13) solutions. 67

4.3. Apparent optical band gaps of iron and iron/chromium alloy films passivated at + 0.9 V in borate buffer solution. 77

4.4. Flat band potentials of iron and iron/chromium alloy films passivated at + 0.9 V in borate buffer solution. 77

5.1. Structure parameters around an Fe atom in $\alpha-Fe_2O_3$ [71]. 83

5.2. Structure parameters around an Fe atom in $\alpha-FeOOH$ [71]. 85

5.3. Structure parameters around a Cr atom in $\alpha-Cr_2O_3$ [72]. 85

5.4. Structure parameters obtained from *in-situ* measurements for Fe and Fe/Cr alloys passivated in 0.1 M $NaNO_2$ by simple immersion. The parameters for $\gamma-FeOOH$ are also shown. 89

5.5. Structure parameters obtained from *ex-situ* measurements for samples passivated in 0.1 M $NaNO_2$ solution. 89

5.6. Structure parameters obtained from *in-situ* measurements for samples passivated in 0.005 M K_2CrO_4. 93

5.7. Structure parameters obtained for $Cr(OH)_3$ compound, Fe foil and film samples passivated in 0.005 M K_2CrO_4 by simple immersion. The measurements were made *ex-situ*. 97

5.8. Structure parameters obtained both *in-situ* and *ex-situ* for the Cr phase in Fe25%Cr alloys passivated in 0.1 M $NaNO_3$. 102

5.9. Structure parameters obtained *in-situ* for Fe and Fe25%Cr samples passivated electrochemically at + 0.9 V in both the borate buffer and 0.1 M $NaClO_4$ solution. Those obtained *ex-situ* for FeOOH samples electrochemically deposited from borate and $(NH_4)_2SO_4$ solutions containing Fe^{2+} ions are also shown. 106

Acknowledgements

I wish to express my gratitude to Dr. J. Robinson for his guidance and his excellent supervision throughout the course of this work.

I am very grateful to Prof. A.J. Forty who introduced me initially to this work and the Chairman of the Physics Department, Dr. H. Mykura, for allowing me to use the facilities at the department.

I would like to thank everyone who helped me in the department; principally my colleagues in the Surface Physics group. I am grateful to the technical staff of the department for their assistance particularly Mr. R.I. Johnston and Mr. P.I. Beecraft.

I am indebted to Mr. Z.K. Chahmana and my family principally my wife Fadila for their continuous and generous encouragement.

I would also like to acknowledge gratefully the Algerian Government for the financial support.

My thanks are also due to the Director of Daresbury Laboratory and SERC for the provision of the synchrotron radiation.

Declaration

This thesis is submitted to the University of Warwick for admission to the degree of Doctor of Philosophy. It contains an account of my work carried out principally at the Department of Physics in the University of Warwick during the period October 1986 to December 1989 under the supervision of Dr. J. Robinson. No part of this thesis has been used previously in an application submitted to this or any other university. The work described is the result of my own independent research except where specifically acknowledged in the text.

M. KERKAR

Abstract

The Electrochemical Polarisation, Photocurrent Spectroscopy and Extended X-ray Absorption Fine Structure (EXAFS) techniques have been used to study the passive film on pure iron and iron alloy samples containing up to 25% chromium. The material used in this work was prepared both as bulk and thin films. The bulk samples were passivated electrochemically at various anodic potentials whereas the film ones were either fully converted into passive films by simple immersion in various solutions for one week or electrochemically at various anodic potentials. The Fe and Fe/Cr film samples used in the electrochemical passivation were deposited onto gold substrate and those passivated by immersion were deposited directly onto mylar.

Polarisation curves for both the bulk and film materials were recorded. They suggest that the electrochemical behaviour of the two materials is similar. The wavelength and potential dependence of the photocurrent spectra were also recorded for the bulk and film samples of Fe and Fe/Cr alloys. The data were analysed to obtain the effective optical band gaps and flat band potentials of the passive films respectively. These results also show that the two materials are similar. Furthermore, the photocurrent data suggest that the passive film on Fe/Cr alloys consists of Fe(III) and Cr(III) phases.

The fluorescence EXAFS above the Fe and Cr K-absorption edges of the passive film on Fe and Fe/Cr alloy films has been recorded both *in-situ* and *ex-situ*. The spectra obtained in these studies were analysed to obtain average Fe-O and Fe-Fe separations as well as Cr-O and Cr-Cr ones. These results together with a detailed examination of the XANES suggest that the passive film on iron in the absence of chromium is best described as a disordered γ−FeOOH-like structure and that on Fe/Cr alloys as well as on pure Fe passivated in chromate solution contains two simultaneous phases of disordered γ−FeOOH and $Cr(OH)_3$. The structure of the chromium containing phase of the passive film was found to be independent of the source of chromium whether it was present in the alloy or it was incorporated from the passivating solution. The EXAFS data show also that the structure of the passive film is insensitive to drying.

The results obtained in these studies have enabled the determination of the structure of the passive film on iron and iron/chromium alloys and the rôle played by chromium in improving the corrosion resistance of iron and its alloys has been identified. These conclusions are discussed in the light of other structural investigations of the passive film.

Chapter 1

General Introduction

1.1 Iron and its Alloys in Engineering

Iron is one of the most abundant elements and it is probably the most common of all metals used by man. Metallic iron has existed for thousands years and was one of the basic materials of the industrial revolution. In spite of the more recent development of other metals and non-metallic substances such as plastics and ceramics, iron remains the material of construction for an extremely large number of purposes.

Iron is manufactured in various forms capable of performing various tasks. The commercial forms of iron are wrought iron, cast iron and steel. Wrought iron is basically pure iron mixed with slag. This slag helps to give the iron some of its useful properties such as ductility and easy shaping hot or cold. Wrought iron is fairly tough, resistant to fatigue and resists corrosion very well.

Cast iron is an alloy of iron, carbon and other elements, the principal one being carbon, which is present in quantities of 2 to 4%. Cast iron cannot be forged or rolled, either hot or cold, but it can be melted and cast into moulds to form various shapes some of which are very difficult to make by other means. It is very weak in tension but very strong in compression. It is also resistant to corrosion. Cast iron is not ductile and breaks suddenly under load.

Steel is an alloy of iron, carbon and other elements, but contains less carbon than cast iron and more than wrought iron. Steel can be made in many different forms, each with its own special characteristics. The most widely used steel in engineering purposes is mild steel which contains up to about 0.25% carbon and as little of other elements as possible.

A steel of carbon content higher than 0.25% can have its physical properties changed considerably. These properties such as hardening are mainly controlled by heat treatments. Many valuable and special properties can also be given to steel. These properties are usually achieved by adding other elements in suitable amounts. For instance, manganese can be used to give steel toughness and make it resistant to abrasive wear.

A major problem with iron and steels is corrosion. It is one of the problems of everyday life since the vast majority of goods and engineering constructions are based on iron and its alloys, which last for only a limited period of time. The losses of these materials as corrosion products in Great Britain alone are estimated at billions of pounds each year, hence, an understanding of corrosion in order to control it is essential.

1.2 General Corrosion

1.2.1 Electrochemical Nature of the Corrosion

Corrosion is the attack of metals by their environments and is electrochemical in nature. Probably the best example to illustrate this is corrosion at the contact between two dissimilar metals. Fig. 1.1 shows two pieces of iron and copper in electrical contact put in a salt solution containing oxygen. As copper is more electronegative than iron, electrons flow from iron to copper and anodic and cathodic reactions take place at the iron and copper surfaces respectively. The anodic metal suffers corrosion whilst the cathodic one remains protected.

Anodic and cathodic areas could be present within a non-homogeneous metal and the metal could provide its own e.m.f. In this case the attack is usually controlled by the rate

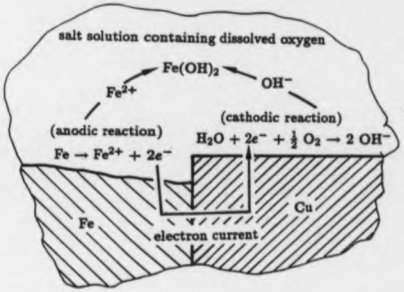

Fig. 1. 1. A schematic illustration of typical electrochemical corrosion without applied e. m. f.

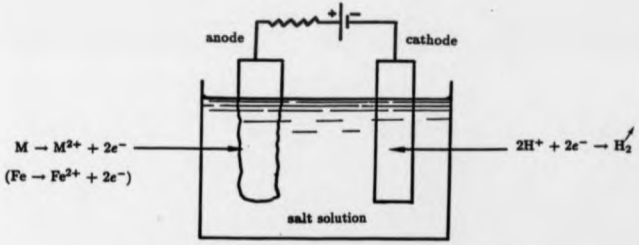

Fig. 1. 2. A schematic representation of a cathodic protection.

at which oxygen can reach the cathodic area.

Another case to consider is two similar metal plates dipping in a salt solution and connected to an external battery (Fig. 1.2). In the absence of passivity the anode will suffer corrosion whilst the cathode will remain protected.

1.2.2 Pourbaix diagrams

Diagrams, with pH and potential as coordinates were first used by Pourbaix to provide information concerning the behaviour of metals in various chemical environments. This graphical method was derived from thermodynamic studies. Fig. 1.3 shows a simplified Pourbaix diagram for iron[1]. The curves present in this diagram represent various chemical and electrochemical equilibria which should exist between iron and aqueous solution. They delimit various regions under which corrosion, passivation or immunity may be expected.

To avoid corrosion the ideal area to choose is the immunity region. In this region corrosion is thermodynamically impossible therefore the polarization of iron leads to its cathodic protection. However, in practice the conditions of immunity are not always adequate especially as in this region water is not stable, it decomposes to give hydrogen at the metal surface.

The alternative way to protect iron from corrosion is to bring it into the passive region. In this area passivity is ensured by the formation of a solid film at the surface which prevents the entry of iron into the solution.

1.2.3 Protection Against Corrosion

In many cases the basic corrosion principles give a good guide to corrosion control. For instance iron could be made to last for a useful period of time by several means such as coating with oils or paints. It can also be protected from corrosion in acid solutions by adding various organic substances. These materials contain nitrogen, sulphur or hydroxyl groups. They act as inhibitors of corrosion by protecting the metal by adsorption. On the other hand

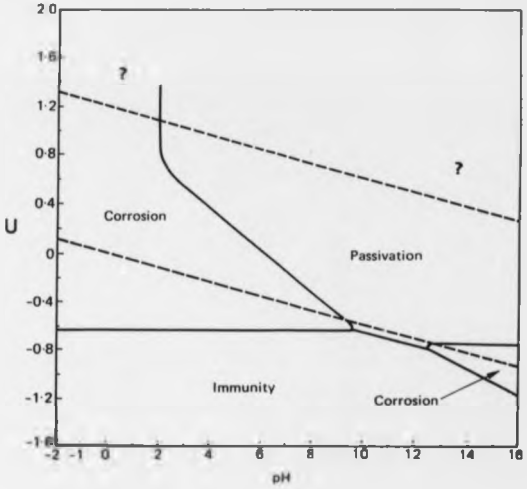

Fig. 1.3. A simplified Pourbaix diagram for iron[1].

inorganic inhibitors such as chromate and nitrate lead to the chemically induced passivity. This passivity has been the subject of extensive experimental and theoretical studies[2].

Cathodic protection is another way of avoiding corrosion. It is used to protect metallic structures in two different ways. One is the use of a sacrificial anode connected directly to the structure and the classical example is the protection of stainless steel water tanks by using a magnesium (Mg) sacrificial anode (Fig. 1. 4). The electronegativity of Mg being lower than that of Fe, Cr and Ni whilst Mg^{2+} ions are safe for human consumption. The same type of protection can be achieved by using an inert anode connected to the structure to be protected via an external source of e. m f. This technique is mainly used to protect large structures such as ships and buried pipelines. In the case of the buried metals, cathodic protection may do damage to other structure within the same soil, therefore, special care must be taken before the use of this kind of protection.

The use of alloying elements is common to increase the corrosion resistance of many metals. Iron-based alloys are especially significant because of the wide use of stainless steel. In stainless steel the corrosion resistance is believed to be due to a formation of a very thin passive oxide film rich in chromium. This film can be formed in various ways such as by exposure to moist air or passivation in solution. The passivation of the metal in aqueous solutions can be achieved either by simple immersion or under potential control. The film is believed to form in stages. First an initial film forms by adsorption of oxygen atoms at the surface then it continues to grow till it reaches a thickness limit of about 50$\AA$ depending on the environment and the nature of the metal. Once this thickness is reached the reaction between metal and oxygen becomes extremely slow, therefore the underlying metal is protected. The film formed on high chromium alloys is thinner than that formed on pure iron metal. In the case of alloys whose chromium content is higher than 18% the thickness of this film is about 20 $\AA$ [3]. Films of this kind are called passive films and their structure is believed to be

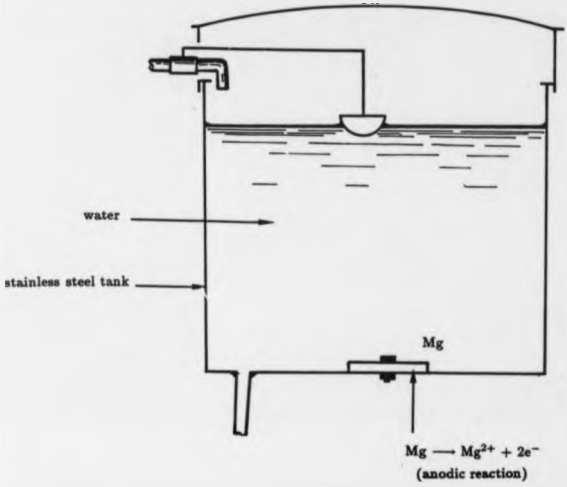

Fig. 1. 4. A schematic representation of corrosion protection with a sacrificial anode.

amorphous. However, very little is known about their structure and composition hence the importance of studying the passive film on iron and iron/chromium alloys.

1.3 Structural Investigation of the Passive Film on Fe and Fe/Cr Alloys by Using Ex-situ and In-situ Techniques

Passive films are usually about 20 to 50 $\AA$ thick, this makes the study of their structure complicated. The amorphousness of these films introduces further difficulties. Studying the structure *in-situ*, as in this work, complicates this still more as water may absorb a significant fraction of the structure probing beam.

The main *ex-situ* techniques that have been used to investigate passive films are electron diffraction and X-ray photoelectron spectroscopy (XPS). The electron diffraction technique can provide information about the structure by measuring the order parameters such as the lattice constant whereas XPS can be used to yield information about the chemical composition of the passive film as well as the chemical environment around one atom within the film. Whilst *ex-situ* studies are in many ways easier than *in-situ* ones, it is unclear how relevant the results are as the samples may have been changed (e.g. undergone a recrystallisation) by the electron beam. Mössbauer spectroscopy and EXAFS techniques can also be used *ex-situ* to investigate the atomic structure of the passive film and have the advantage that they may also be applied *in-situ*.

The *in-situ* spectroscopy techniques are mainly based on optical frequency probes. They can be used to characterise passive films with respect to their electronic and molecular properties. Such techniques are ellipsometry, Raman spectroscopy and photocurrent spectroscopy. In addition to this as we have seen Mössbauer spectroscopy and EXAFS techniques may be used *in-situ* to derive information about the structure of passive films.

1.3.1 Ex-situ Investigations

The most widely used *ex-situ* technique in studying the structure of the passive film is electron diffraction. Nagayama and Cohen[4] obtained an electron diffraction pattern of an anodic passive film on a (112) single crystal of iron in borate buffer. The pattern indicated that the film had a cubic structure with an average lattice parameter of $a = 8.37 \pm 0.04\AA$. As the lattice parameters of γ-Fe_2O_3 and Fe_3O_4 are $8.35 \pm 0.04\AA$ and $8.39 \pm 0.04\AA$ and taking into account their cathodic reduction results they suggested that the outer and inner layers of the passive film are mainly composed of γ-Fe_2O_3 and Fe_3O_4 respectively. Foley *et al*[5] extensively studied the passive film formed anodically on iron foils using selected area transmission electron diffraction. In their experiments the passivation of iron planes with different orientations [(100),(110),(111),(210) and (211)] was studied in 0.1N H_2SO_4, 0.1N NaOH and borate buffer solutions. The passive film gave electron diffraction patterns of γ-Fe_2O_3 regardless of the pH of the solution and these patterns also contained Fe_3O_4 reflections. These results were again interpreted by the presence of an inner Fe_3O_4 and an outer γ-Fe_2O_3 layer. In later investigations however, electron diffraction patterns with no extra reflections due to Fe_3O_4 were obtained by Kuroda *et al*[6] for various specimens, with different orientations, passivated in borate buffer solution at various potentials. These electron diffraction results were not very conclusive because it is not possible to make a definitive distinction between γ-Fe_2O_3 and Fe_3O_4 since their lattice parameters are so similar.

Ex-situ Mössbauer spectroscopic data were obtained by Bratt *et al*[7] for a passive film formed anodically on a film prepared by electrodeposition of ^{57}Fe onto a platinum disc. These data gave Mössbauer parameters which match up with those of γ-Fe_2O_3.

XPS has also been used to investigate the structure of passive films. Konno and Nagyama[8] studied the passive film on iron formed anodically in borate buffer using this technique and they concluded that structure consisted of an inner Fe_3O_4 and an outer γ-Fe_2O_3 layers with

water weakly adsorbed on the surface. However, XPS results obtained by Brett *et al*[7] showed that the composition of these films is strictly dependent on the presence of Fe^{2+} ions in the solution. Films formed in solutions containing Fe^{2+} ions resembled γ-FeOOH whilst those formed in the absence of Fe^{2+} were similar to γ-Fe_2O_3.

EXAFS is one of the direct methods for probing local atomic structures in matter. It has been used *ex-situ* by Long *et al*[9] to study the passive film on iron. Passivity was achieved by immersion of glass slides coated with a thin iron film in either nitrate or chromate solutions for one week. The Fourier transform of the EXAFS data, derived from these samples, gave Fe-O bond distances of $1.91 \pm 0.05\AA$ and $1.99 \pm 0.05\AA$ for the nitrate and chromate passivated films respectively. These distances are situated between Fe-O and Fe-OH distances formed in γ-Fe_2O_3 and γ-FeOOH model compounds. The first Fe-Fe distances obtained for the passivated film were shorter than those obtained for Fe_3O_4 and γ-Fe_2O_3 and similar to that of γ-FeOOH. However, by comparing the EXAFS data the authors suggested the structure of these passive films was best described as a disordered version of γ-Fe_2O_3 oxide. This was supported by the fact that the first and second nearest neighbour distances were slightly different from those of γ-Fe_2O_3 as was the amplitude ratio of the first to the second peak in the Fourier transform. The Fourier transforms of the data derived from the passive films showed a third peak which was attributed to the second Fe-Fe bond distance of the iron substrate arising because their samples were not fully converted into passive films. In their later investigations[10,11] using thinner samples also passivated in nitrite and chromate solutions for one week, they obtained similar results for measurements in air and in an He atmosphere. In this case the third peak was not present and the results were attributed to a disordered form of γ-Fe_2O_3. The bond distances were also found in the case of the chromate passivated film to be higher than in that passivated in nitrite solution. This has been attributed to chromium inclusion into the film from the chromate solution.

Most results derived from *ex-situ* measurements show that the passive film on iron has a similar structure to γ-Fe_2O_3 possibly with an inner layer of Fe_3O_4.

1.3.2 In-situ Investigations

The optical paramaters of the anodic passive film on iron in borate buffer solution (pH 8.4) have been obtained by ellipsometry[12–14]. Szklarska-Smialowska and Kozlowski[12], and Ord[13] have found that the refractive index and the absorption coefficient change with the passivation potential and they concluded that the passive film contained iron in the oxidation states 2+ and 3+. Hence their results supported the duplex model. However, in later investigations using the same technique, Chen and Cahan[14] found that these passive films have optical properties consistent with a simple Fe^{3+} layer. Other ellipsometric measurements have been made on a relatively thick film formed on an iron electrode by galvanostatic cycling in 0.05M NaOH [15]. This investigation has shown that an outer layer of Fe_2O_3 was building up progressively (100 $\AA$ on each cycle) over an inner compact layer of Fe_3O_4 approximately 40 $\AA$ thick. Unlike the outer layer the inner one was removed by cathodic reduction and it was suggested that this layer of Fe_3O_4 acted as a barrier layer for field-limited ionic transport and when reduced on a cathodic cycle it provided the iron which enabled the outer layer to grow on the subsequent cycle. This process shows that this type of film differs from the passive one.

Raman spectroscopy has been used *in-situ* to study the structure of the anodic oxide that forms on iron in different electrolytes[16–19]. However, these spectra were obtained only for films artificially thickened either by long time polarisation (> 12 hours) or by several oxidation-reduction cycles[16]. These films were 100-200 $\AA$ thick and therefore their structure may be very different from that of the passive film which is only about 50 $\AA$ thick. The results of Raman spectroscopy gave evidence for the presence of Fe^{2+} as well as Fe^{3+} oxidation states

which were assigned to Fe_3O_4 and α-FeOOH respectively.

Based on the assumption that the passive film that forms on iron is a semiconductor in nature, a lot of effort has gone into the study of its electronic structure using photocurrent spectroscopy[20-30]. Although results were not obtained that permitted accurate identification of its composition, the analysis of the data enabled the determination of the band gap energy on the assumption that the photo-process was an indirect allowed transition. These data have also been used to derive the absorption spectrum of the anodically produced passive film on iron[20] which has been found to be significantly different from that obtained for crystalline Fe_2O_3 [21]. It was suggested that this was associated with the amorphousness of its structure and this is in agreement with the work by Abrantes and Peter[20] where they found that the photocurrents show a pronounced relaxation effect which is consistent with charge transfer via localized states. Sunseri *et al*[22] used photocurrent spectroscopy to study the passive film on ferrite stainless steels. They found that the effective band gap energy was dependent on the potential at which the film was formed. Nickel was also found to play a role in determining the composition of the film. In the case of low nickel content steels the film formed at low potentials had a band gap energy of 2.5 eV which matches up very well with that of the passive film on chromium metal and as the potential increased the band gap energy decreased. For high anodic potentials the film had a band gap energy of 1.9 eV which suggested that the passive film was mainly iron based oxide. However, as the nickel content exceeded 3.1% the film seemed to be very rich in chromium. Therefore Sunseri *et al*[22] concluded that for low Ni content the composition of the film formed on these steels was probably Cr_2O_3-Fe_2O_3 solid solutions with the composition dependent on the potential of formation. These results suggest the need for information on simpler Fe/Cr alloys for better characterisation of the passive film on stainless steels.

O'Grady[31], using Mössbauer spectroscopy, showed that the passive film on iron formed

anodically in borate buffer solution has an isomer shift consistent with FeOOH but its quadrupole splitting does not match up with any of those of stoichiometric oxides or hydroxides. This has been attributed to amorphous iron(III) oxides, iron containing polymers, and bi-nuclear iron compounds containing di-oxy and di-hydroxy bridging bonds between the iron atoms. The results obtained in these studies at low temperature show that the film is amorphous and polymeric in nature. However, an extensive drying of the passive film caused irreversible changes in the structure. The dehydrated film gave Mössbauer parameters that match up with those of γ-Fe_2O_3.

In recent years EXAFS has been used *in-situ* to study the structure of the passive film on iron. Kruger *et al*[11] and Long *et al*[9] have reported Fe-O bond distances of $2.01 \pm 0.06\AA$ and $2.08 \pm 0.06\AA$ for nitrate and chromate passivated films on glass substrate. These bond distances match up well with those of a γ-FeOOH model compound. However, the first Fe-Fe bond distance derived from the passive film were found larger than that derived from γ-FeOOH and shorter than that derived from γ-Fe_2O_3 model compounds. This has been explained by the accommodation of some hydrogen-containing species into the structure of the passive film. This deduction was in agreement with that of O'Grady[31]. Together with the near edge structure results this was used to suggest that the *in-situ* passive film is not a simple ferric oxy-hydroxide, but that hydroxide or water are probably also constituents of the passive film. Here again the film formed in chromate solution gave bond distances larger than that passivated in nitrite which has been attributed to the inclusion of chromium in the film increasing the amorphousness of the structure. Preliminary *in-situ* EXAFS spectra have already been obtained for the potentiostatically controlled passivation of iron in borate buffer solution (pH 8.4) by using various cell designs[32,33]. However, the data were not analysed properly therefore no conclusive results concerning the structure of the electrochemically passivated film were achieved.

The results of *in-situ* investigations stated above are different from the *ex-situ* ones. They suggest that water has a significant effect on the structure of the passive film.

1.3.3 Summary

Over many years there has been much debate about the structure of the passive film that forms on iron and the subject still remains controversial. A number of models have been put forward[34–39] but the most accepted one is the duplex model. According to this the passive film on iron consists of an inner layer of crystalline Fe_3O_4 at the metal/oxide interface and an outer layer of γ-Fe_2O_3. The argument for this model is that it is not possible thermodynamically for a film which consist of iron in the Fe^{3+} oxidation state to be in direct contact with metallic iron and the passive film is believed to be basically an Fe^{2+} oxide.

The *ex-situ* measurements outlined earlier using different techniques such as electron diffraction[4–6] have supported the duplex model. It must be remembered however that the results of the *ex-situ* experiments could be influenced by the removal of water from the films when exposed to air or transferred to a vacuum environment as well as electron beam damage which could cause their restructuring.

Some of the *in-situ* investigations have also supported the duplex model[12,13,15–18]. However, in recent Mössbauer[7,31] and EXAFS[9,11] investigations the passive film on iron was found to be a single phase structure. In these investigations water has been found to play a major role in the structure of the passive film on iron. This structure was shown to be disordered and polymeric in nature with amorphous iron(III) oxide or hydroxyde similarities.

Clearly despite all this previous work there is still a need for further studies to settle this problem.

1.4 The Aim of the Work Reported in this Thesis

The aim of the work reported in this thesis is to model the structure of the passive films that form on pure Fe and Fe/Cr alloys. For this purpose the EXAFS technique was chosen since it can probe the local atomic structure of both crystalline and amorphous materials. Transmission and fluorescence EXAFS techniques can be used both *ex-situ* and *in-situ* to study high atomic number elements such as Cr and Fe which are 24 and 26 respectively. However, for dilute systems fluorescence is more sensitive than the transmission mode making it particularly useful for the study of passive films since their thickness does not exceed 50 $\AA$. Therefore in these experiments fluorescence EXAFS was measured above the Fe and Cr K-absorption edges. This has the advantage of restricting the nearest neighbour bond length measurements to either Fe-O and Fe-Fe or Cr-O and Cr-Cr distances for the absorption fine structure measured above the Fe or Cr K-absorption edge. Therefore only the local geometrical structure around either Fe or Cr is investigated. In addition to this X-ray absorption spectra were measured in a transmission mode for model compounds.

The EXAFS measurements made in this present work were performed on fully converted thin Fe and Fe/Cr alloy films to passive ones. The Fe and Fe/Cr alloy films were formed by vapour deposition either directly on clean mylar or on gold on mylar substrates. There is therefore a need for the characterisation of the passive film on this material as it may differ from that formed on bulk. For this polarisation curves for both the bulk and film materials were recorded. The photocurrent spectroscopy technique was also used to characterise these films. This technique provides useful additional information such as their optical band gap energies and flat band potentials as these films show a semiconducting behaviour. This information was used to support the EXAFS data in modelling the structure of the passive films formed on Fe and Fe/Cr alloys in the present work.

1.5 Plan of the Thesis

Photocurrent spectroscopy and EXAFS techniques were used in the present work to investigate the structure of the passive films that form on iron and iron/chromium alloys. The remaining part of this thesis is divided into five chapters.

Chapter 2 is devoted to a brief description of the theory of both photocurrent spectroscopy and EXAFS. In this chapter an account is also given of the methods used to derive electronic and structural information from the photocurrent and EXAFS data respectively. In the next chapter signal detection, experimental apparatus and the preparation of glassware, solutions and electrodes are described for both techniques. The experimental procedures are also described. The photocurrent spectroscopy results are presented and discussed in chapter 4 whilst those of EXAFS are dealt with in chapter 5. Finally, conclusions about the structure of the passive films on iron and iron/chromium alloys are given in chapter 6.

Chapter 2

Techniques Used for Studying Passivated Films of Fe and Fe/Cr Alloys

2.1 Introduction

This chapter is concerned with the two different techniques used in this work to study the passive films on Fe and Fe/Cr alloys. These techniques are photocurrent spectroscopy and extended X-ray absorption fine structure (EXAFS). By using the photocurrent spectroscopy technique, these films can be characterised with respect to their electronic structure whilst EXAFS is used to provide information concerning their local atomic environment. It is therefore convenient to present these techniques into two separate sections.

2.2 Photocurrent Spectroscopy

2.2.1 Introduction

Since the identification of the passive films that form on transition metals as semiconducting materials[40], photoelectrochemistry became one of the tools for studying the electronic properties of these materials.

If a passive film absorbs light of higher energy than its band gap, electrons can be excited

from occupied electronic states into unoccupied ones leaving holes behind. The creation of electron hole pair

$$h\nu \longrightarrow e^- + h^+ \qquad (2.1)$$

causes a change of the charge distribution in the film which can result in a current when electrons or holes react with acceptor or donor states respectively at the film/solution interface.

The passive film can be an n-type, or p-type, semiconductor, or an insulator. The n-type semiconductor can be distinguished from the p-type by the relative positions of the conduction band and Fermi level. In an n-type semiconductor the Fermi level lies just below the conduction band in the band gap whereas in the p-type the Fermi level is just above the valence band. A non-illuminated semiconductor before its contact with a solution has flat bands but in an electrolyte solution these bands are bent according to its conduction type. This band bending is illustrated in Fig. 2. 1. For example in the case of an n-type semiconductor where the Fermi level is higher than that of the redox couple in the solution charge transfer between the solution and the semiconductor can occur only if electrostatic equilibrium is attained this is to say that the Fermi levels must become equal. In this case the bands are bent upwards. Under illumination (Fig. 2. 1) if a photon is absorbed and an electron hole pair formed they are separated in the electric field of the space charge layer. The hole migrates to the solution interface reacting with an occupied state (donor) whilst the electron flows to the back contact and the resulting photocurrent is anodic. On the other hand for a p-type semiconducting film (again with a Fermi level higher than that of the redox couple) the situation is reversed and the bands are bent downwards. The electron moves to the surface where it can react with an unoccupied state (acceptor) whilst the hole flows to the back side contact (Fig. 2. 1) and the resulting photocurrent is cathodic. In the case of an insulating film the sign of the electric field in the film forces the photocurrent to become either cathodic or anodic since the potential gradient in an insulating film is constant.

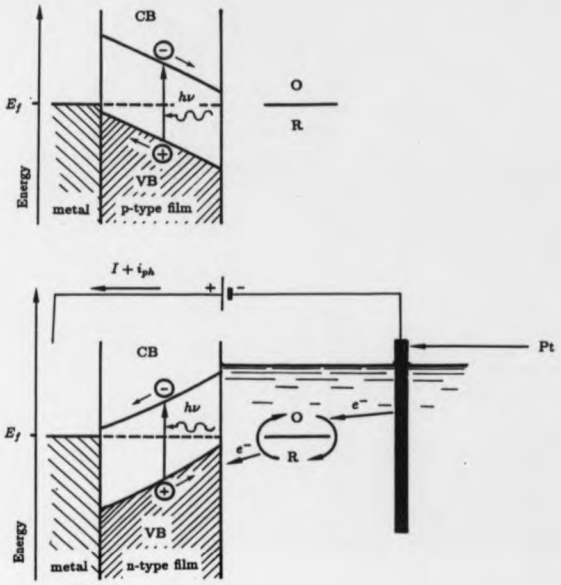

Fig. 2. 1. A schematic diagram of illuminated p-type and n-type passive films under depletion conditions. The photoelectrochemical reaction for an n-type film is also illustrated.

The sign of the photocurrent in semiconducting films changes with the sign change of the electric field. This sign change occurs at potential at which the bands become flat, known as the flat band potentials (U_{fb}).

2.2.2 Theory of Photocurrent Spectroscopy

Up till now there is no theory of the photocurrent spectroscopy for amorphous semiconductors. However, it is well established that the theory obtained for crystalline semiconductors is an accepted way of describing the photochemical behaviour of amorphous films.

The photocurrent generated during a photochemical process at a crystalline semiconductor, ignoring any recombination, may be written as[41,42]

$$i_{ph} = e\eta I_0\{1 - \exp[-\alpha d_{sc}(\varepsilon/kT)^{1/2}(U - U_{fb})^{1/2}]/(1 + \alpha L)\}, \tag{2.2}$$

where e is the electronic charge, η the quantum efficiency, I_0 the incident photon flux, α the absorption coefficient, U the potential of the electrode, U_{fb} the flat band potential, L the diffusion length of the minority carriers and d_{sc} the Debye length. The Debye length is expressed by

$$d_{sc} = (\frac{\varepsilon\varepsilon_0 kT}{e^2 N})^{1/2}, \tag{2.3}$$

where ε is the dielectric constant and N the concentration of the minority carriers. The diffusion length is given by

$$L = (D\tau)^{1/2}, \tag{2.4}$$

where D and τ are the diffusion coefficient and the life time of the minority carriers respectively.

The information that is contained in the photocurrent generated from a passive film is concerned with its electronic properties which are basically the band gap (E_g) and the flat band potential (U_{fb}). In the next two sections a brief account on the theory of the wave

length and the potential dependence of the photocurrent is given and for more details the reader is referred to a paper by Stimming[43].

2.2.2.1. Wave Length Dependence of the Photocurrent

Leitner *et al*[44] used the absorption data for TiO_2 [45] to calculate the number of absorbed photons by means of

$$N_{ph} \propto 1 - e^{-\alpha d} \tag{2.5}$$

and found that for photon energies close to the band gap energy for very thin films (up to 1000 $\AA$), N_{ph} becomes linearly dependent on d. Therefore for lower α and d the photocurrent, i_{ph}, also becomes proportional to α. Knowing that for crystalline material the absorption coefficient α can be written as[43]

$$\alpha = A(h\nu - E_g)^n/h\nu \tag{2.6}$$

the energy gap E_g can be easily evaluated from $(i_{ph}.h\nu)^n$ vs. $h\nu$ plots. The value of n is dependent on the type of the observed transition. The most likely transitions to be observed are either direct or indirect ones where $n = 2$ and $n = \frac{1}{2}$ respectively[46,47]. Therefore by using these values of n the values of the band gap energy, E_g^d or E_g^i, can be obtained for the direct or indirect transitions respectively. For thin enough films, for which $i_{ph} \propto \alpha$ holds, photocurrent spectra can be also used to determine the type of the transition.

2.2.2.2. Potential Dependence of the Photocurrent

By maintaining the wavelength constant the absorption coefficient is a constant and therefore the photocurrent becomes potential dependent. For $\alpha d_{sc}(e/kT)^{1/2}(U - U_{fb})^{1/2} \ll 1$ the exponential function in equation (2.2) can be expanded[43] and the photocurrent can be written as

$$i_{ph} = \text{Const.}(U - U_{fb})^{1/2} \tag{2.7}$$

with Const.$= e\eta I_0 d_{sc}(e/kT)^{1/2}$. Therefore i_{ph}^2 vs. U plots should be straight lines and the extrapolation to $i_{ph} = 0$ should yield the flat band potential U_{fb}. The flat band potential can also be identified as the value U_0 for $i_{ph} = 0$ on the i_{ph} vs. U plots. These plots can be used in conjunction with the value of the flat band potential to identify the nature of passive films such as amorphousness and the presence of mixed phases.

2.3 Extended X-ray Absorption Fine Structure (EXAFS)

2.3.1 Introduction

EXAFS is a direct method and a powerful tool for probing the local atomic environment for all states of matter other than monatomic gases. It has been established recently as a useful technique for investigating the structure of amorphous solids.

X-ray absorption in matter is characterized by a sharp rise corresponding to the absorption edge where a core electron can just be excited to above the Fermi energy. This leaves the absorbing atom ionised. The edge energy corresponds to a a particular core shell threshold energy. The excitation of the deepest, 1s, shell corresponds to the K-edge and progressively less energetic transitions that involve the excitation of 2s, $2p^{1/2}$ and $2p^{3/2}$ are known as the L_I, L_{II} and L_{III} edges respectively. A measurement of the absorption coefficient for condensed matter above the absorption edge as a function of energy reveals oscillations which contain structural information about the material under investigation. These oscillations extend for several hundreds of electron volts, hence their description as the extended X-ray absorption fine structure (EXAFS).

Since each element has its own absorption edge it is possible to study the pair correlations around one kind of element in the presence of others by monitoring the EXAFS at an X-ray energy above its characteristic absorption edge. However, to achieve this a tunable high power source of X-rays is needed. Nowadays this is made possible by the availability of synchrotron

radiation sources in the form of high-energy electron storage rings which can provide a high flux of white X-rays. For example the Daresbury SRS produces radiation with a flux of 3×10^{13} photons s^{-1}/mrad horisontal/0.1% bandwidth at a wavelength of 1.5 $\AA$.

An X-ray absorption measurement gives a spectrum consisting of three different regions. As shown in Fig. 2.2, the first region is the pre-edge which corresponds to the relatively low absorption background. The second region locates the absorption edge where the X-ray absorption near-edge structure (XANES) may be identified, and finally, the third region, above the absorption edge, consists of the fine structure which extends, as mentioned above, for several hundred eV (usually between 400 and 1000 eV above the absorption edge).

The mechanism that gives rise to the EXAFS is illustrated in Fig. 2.3. When an X-ray photon is absorbed by an atom it is accompanied by the release of a photoelectron wave which spreads outwards. Parts of this outgoing wave are backscattered from the surrounding atoms and interference can occur between the outgoing and the backscattered waves. This interference causes the modulation of the absorption cross-section.

2.3.2 Theory of EXAFS

The fine structure above the absorption edge may be defined by

$$\chi(k) = \frac{\mu(k) - \mu_0(k)}{\mu_0(k)} \tag{2.8}$$

where $\mu(k)$ is the absorption of the sample and $\mu_0(k)$ is the absorption coefficient of an isolated atom with no neighbours. These absorption coefficients are both due to the excitation of an electron from a single core level of an atom under investigation. The theory of EXAFS has been developed by several workers, for example Sayers *et al* (1971)[48] Lee and Pendry (1975)[49]. The idea is that, for example, in a solid the atom is surrounded by other atoms and the outgoing photoelectron wave caused when an X-ray photon is absorbed by an atom will be scattered by the neighbouring atoms. The surrounding atoms are regarded as a system of

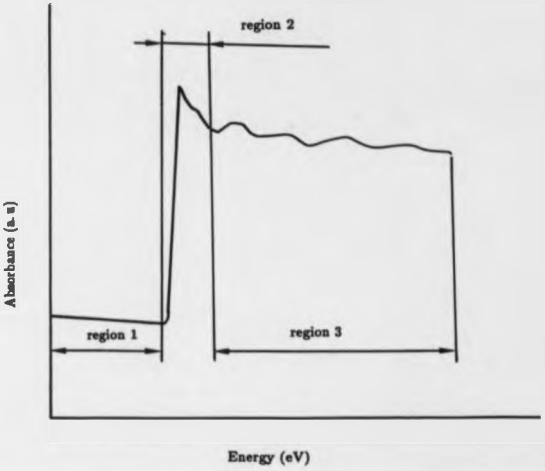

Fig. 2. 2. An X-ray absorption spectrum showing the three different regions.

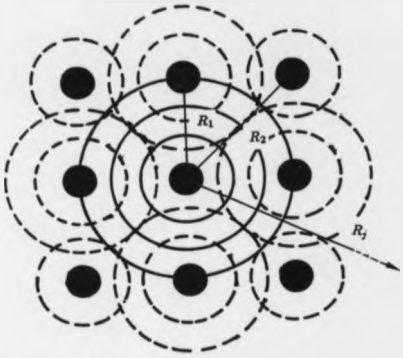

Fig. 2. 3. Modulation of the absorption cross-section leading to EXAFS. The solid lines represent the outgoing photoelectron wave, whereas the dashed lines represent the back-scattered wave.

weak point-scatterers. This leads to the description of the EXAFS in terms of standard single scattering theory. The formalism used by Sayers *et al*[48] and other workers is represented by the following equation for $\chi(k)$ expressed in momentum-space

$$\chi(k) = \sum_j \frac{N_j}{kR_j^2} \exp(-2\sigma_j^2 k^2) \mid f_j(\pi, k) \mid \exp(-2R_j/\lambda_j) \sin(2kR_j + \Phi_j(k)) \qquad (2.9)$$

where N_j is the number of neighbouring atoms in the j^{th} shell situated at a distance R_j from the absorbing atom. The summation in $\chi(k)$ is over all neighbouring shells. Φ_j is the total phase shift experienced by the photoelectron wave in leaving the absorbing atom and being backscattered from each of the neighbouring atoms. This can be expressed as

$$\Phi_j(k) = \xi_j(k) + 2\delta_l. \qquad (2.10)$$

δ_l represents the phase shift, for the angular momentum $l = 1$, due to the absorbing atom which is counted twice because both the outgoing and backscattered electron waves experience this shift. $\xi_j(k)$ is the phase of the backscattering amplitude from each of N_j neighbouring atoms in the j^{th} shell which is given by

$$\mid f_j(\pi, k) \mid = F_j(\pi, k) e^{i\xi_j(k)} \qquad (2.11)$$

The thermal vibration of the atoms has the effect of smearing out the EXAFS oscillations $\chi(k)$ [50]. The displacement of the atoms due to the thermal vibration, structural disorder and other factors are introduced in the equation (2.9) by the Debye-Waller factor $[\exp(-2\sigma_j^2 k^2)]$, where σ_j^2 represents the mean square amplitude of the relative displacement of the atoms in j^{th} shell from the absorbing atom. For a given material σ_j^2 corresponding to the amorphous state is greater than σ_j^2 for the crystalline state[51]. This is because the static disorder in amorphous materials is greater than the static disorder in crystalline materials. Therefore there is a greater spread of distances from the absorbing atom to the atoms of the j^{th} shell in amorphous materials. The factor $\exp(-2R_j/\lambda_j)$ describes the decay of the photoelectron wave due to inelastic scattering (mean free path $\lambda(k)$) of the photoelectrons.

The wave vector of the photoelectron (k) is defined by

$$k = \frac{\sqrt{2m_e}}{\hbar}(E - E_0)^{1/2} \tag{2.12}$$

where m_e is the mass of the electron, $\hbar$ is Planck's constant divided by 2π, ($\hbar = \frac{h}{2\pi}$), $E = h\nu$ is the photon energy and E_0 is the threshold energy which is taken as the zero reference in the EXAFS energy scale. The value of E_0 is not easy to identify precisely. It is therefore approximated within a few eV by adjusting it to the energy corresponding to the half-height point on the absorption edge of the EXAFS spectrum[52,53]. The value of E_0 corresponds to the energy level from which the electron emerges from the atom and it is often taken to be just below the Fermi level in metals. This approximation does not introduce any problem since it can be corrected easily in later stages of the analysis.

2.3.3 Extraction of Structural Information from EXAFS

The EXAFS spectra contain information about the structure of the material under investigation. The analysis of the EXAFS data starts first by extracting the EXAFS oscillation function, $\chi(k)$, which will be discussed later in section 5.2.2. This function is a superposition of terms of the form $\sin(2kR_j)$ which corresponds to damped sine-waves. The Fourier transform of this will produce peaks at the atom positions (R_j) in real space. The fine structure extends to a few hundred of eV above the absorption edge instead of extending from 0 to ∞. The actual limits of this in k-space are $k \simeq 3\ \text{Å}^{-1}$ and $k \simeq 20\ \text{Å}^{-1}$. This is due to the effect of both the Debye-Waller term, the decay of the photoelectron wave which causes a decrease in the backscattering amplitude with k and, in practice, the presence of neighbouring absorption edges. These limits make the theory uncertain so one has to measure the fine structure over as wide a range of energies as possible. $\chi(k)$ is chosen to be extended from a value of $k_{min} \simeq 1 - 4\ \text{Å}^{-1}$ to k_{max} depending on the data under consideration. The value of k_{min} corresponds to an energy of 20 to 60 eV above the absorption edge. The oscillation function

$\chi(k)$ is usually multiplied by factor k^n which compensates for the rapid attenuation of the backscattered amplitude $|f_j(\pi,k)|$ at large values of k. This has the effect of weighting the EXAFS oscillations with some degree of uniformity over a range of k. Since the backscattering cross-section increases from light to heavy elements the power of the weighting factor (k^n) is chosen as follows[54]

$$n = 1 \qquad Z > 37$$

$$n = 2 \qquad 19 \leq Z \leq 36$$

$$n = 3 \qquad Z \leq 18.$$

The quality of the EXAFS data are also used in practice as a criterion in the choice of the weighting factor. Thus n varies from 1 to 3 and one should use the value by which a more or less uniform amplitude of the data is obtained. By considering the factors cited above, the Fourier transform may be expressed as

$$F(R) = \frac{1}{2\pi}\int_{k_{min}}^{k_{max}} w(k)\chi(k)k^n \exp(-2ikR)dk \qquad (2.13)$$

where $w(k)$ is a window function[55] used to overcome the data truncation effect. This Fourier transform should peak at distances corresponding to the atomic shell distances which are shifted towards the origin as a result of the phase shifts $\Phi_j(k)$. There is therefore a need to correct for these phase shifts before the correct values of bond lengths are obtained.

There are two different approaches to correct values of R obtained from Fourier transforms. The classical one is the use of Teo and Lee tabulated phase shifts[54] or by comparing the Fourier transform of the model compound with its X-ray crystallographic data. The difference should yield the correction factor ΔR which can be used to correct the interatomic distances of the unknown compound based on the same elements as the model one. The more modern approach to the structure is to calculate a curve that fits EXAFS in k-space by using either the plane[48] or curved[56] wave theories. In this present work the data analysis

was achieved by calculating EXAFS using the exact curved wave theory[56]. This required a phase shifts calculation which was refined by using a good model compounds.

2.3.4 The Phase Shift Determination

Phase shifts are obtained by calculation using MUFFPOT program[57]. The program calculates phase shifts files for each element of the compound starting from the absorbing atom then it calculates the phase shifts for the backscattering atoms. By using a model compound of the same elements as the system under investigation whose structure is well known from X-ray diffraction, these phase shift files were then refined to get new phase shift files. The procedure started by refining E_0 then the phase parameters, the data file for parameters being that derived from X-ray diffraction. When a good fit was obtained new phase shift files were printed. These phase shift files were used to test the transferability of the phase shift by using other model compounds which consisted of the same elements. The good fit obtained with the structure suggested by X-ray diffraction demonstrated the transferability of the phase shift. These phase shift files and the value of E_0 obtained for the model compound were used to compute EXAFS using the curved wave theory[56] for different models and by comparison with the experimental EXAFS data structural information were obtained. This method yields information with great accuracy, however, the phase shift determination requires a good model compound and the calculations are computer-intensive.

2.3.5 General Methods of Measuring EXAFS

Several techniques can be used for measuring the extended X-ray absorption fine structure. These techniques are based on either direct or indirect measurements of the X-ray absorption coefficient, μ, and include using X-ray transmission, X-ray fluorescence and electron yield to monitor the absorption. The only direct method is that based on transmission measurements, all the rest are indirect. In this section a brief account of the various methods is given.

2.3.5.1. Transmission EXAFS

The simplest, and earliest, experimental technique for measuring an EXAFS spectrum is the transmission method. This is illustrated in Fig. 2.4, where an X-ray beam, having an intensity I_0, passes through a thin sample is attenuated by absorption and its intensity, I_t, can be measured using ionisation chambers (or other means). Two ionisation chambers are thus required in the experimental arrangement. One, placed in front of the sample (see Fig. 2.5) measures I_0, while another chamber, placed behind the sample measures the I_t that passes through the sample. It is found that

$$I_t = I_0 \exp(-\mu x) \tag{2.14}$$

or

$$\mu_x = l_n(I_0/I_t)$$

where μ is the X-ray absorption coefficient and x is the sample thickness.

The optimum value for the thickness of a sample for a transmission measurement is determined using the following criterion[58]

$$x = 1.2/\mu \quad (\mu m) \tag{2.15}$$

This corresponds to a reduction of the incident intensity by one-third. Since $\mu < 1\ \mu m^{-1}$, in any sample the thickness is at least a few microns, therefore the transmission EXAFS technique is not ideal for investigating the structure of thin films which are often less than a micron thick.

2.3.5.2. Fluorescence EXAFS

An excited atom relaxing back to its ground state may release fluorescent radiation. As illustrated in Fig. 2.6a, fluorescence is the emission of a photon when an excited atom is

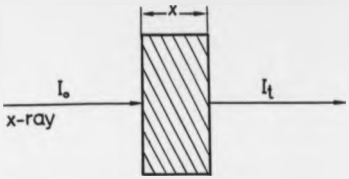

Fig. 2. 4. A schematic diagram of transmission of an X-ray beam through a sample of a given thickness *x*.

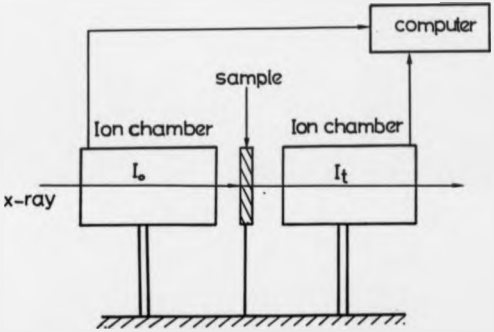

Fig. 2. 5. A schematic diagram of the experimental arrangement for recording the transmission EXAFS.

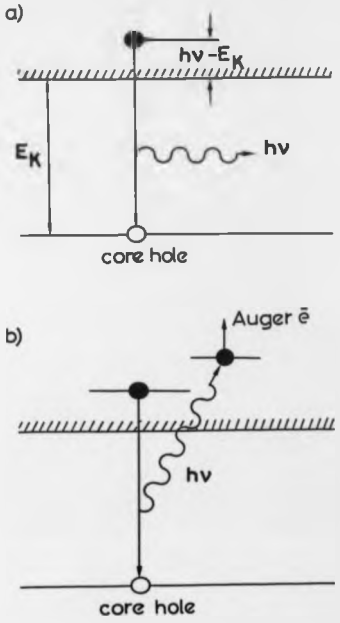

Fig. 2. 6. A schematic diagram of (a) fluorescence and (b) Auger emissions when an excited state relaxes.

returning to its ground state as an electron drops in energy to fill the core hole. This radiation is less energetic than the exciting radiation and their characteristic energies are independent.

The fluorescent radiation is detected for example by means of an array of scintillation detectors placed around the sample[59] or an array of solid state detectors as will be stated later in chapter 3. The intensity of the incident X-ray beam is measured by an ionisation chamber and the fluorescence intensity is normalised to it.

The fluorescence EXAFS mode is particularly useful for dilute systems specifically for materials of medium to high atomic number such as iron ($Z = 26$) and chromium ($Z = 24$). This mode was therefore chosen in this work.

2.3.5.3. Electron Yield EXAFS

The electron yield EXAFS technique has played an important role in the study of surface atomic arrangements and thin surface films such as metallic oxides. There are two methods for measuring electron yield EXAFS; Auger electron yield EXAFS and the total electron yield EXAFS.

The Auger electron emission is an alternative mode of relaxation of an excited atom to that which occurs in fluorescence emission. As illustrated in Fig. 2.6b, a bound electron of a fixed initial energy undergoes a transition to fill the core hole. During this transition the electron loses its energy by transferring it through Coulomb interactions to another electron which is excited out from the atom. The electron is then detected and the Auger electron yield can be measured by using energy discriminating detectors (for example, a hemispherical or cylindrical electron energy analyser).

In the case of the total electron yield EXAFS, all electrons emitted from the surface of the sample are collected regardless of their kinetic energy. These electrons are elastic photoelectrons, elastic electrons originating from the recombination process, and inelastically

scattered electrons which are dominant. The total electron yield EXAFS is usually measured by using a channeltron electron multiplier. This mode generally requires high vacuum or at least an He atmosphere therefore it is not suited to the *in-situ* work.

Chapter 3

Experimental

3.1 Introduction

This chapter is divided into two parts. The first part describes the photocurrent spectroscopy experiment whilst the second one is devoted to the X-ray absorption spectroscopy experiment.

3.2 Photocurrent Spectroscopy Experiment

3.2.1 Introduction

Photocurrents were measured in this work by using a chopping technique in conjunction with phase sensitive detection. The principles of this signal detection method are therefore considered here. The rest of this part of the chapter is devoted to the description of the experimental apparatus, preparation of glassware, solutions and electrodes. The experimental procedure is also described.

3.2.2 Signal Detection

A phase sensitive detector (psd) was used in this work to measure the small photocurrent generated by illumination of passivated metallic electrodes under potential control. Phase

sensitive detectors are usually used to separate a.c. signals obscured by high noise levels or to measure accurately very small signals in the presence of lower noise levels.

A simplified block diagram of a psd is shown in Fig. 3.1. It consists of a signal input channel, a reference input channel, a demodulator and a low pass filter. The demodulator is driven by a reference signal which is in phase with a signal to be measured. The reference channel incorporates a phase shifter enabling compensation for phase shifts in the electrochemical equipment. The output of the demodulator passes then through a low pass filter for primary noise attenuation. This effect being variable by the time constant control. The psd is operating by multiplying the input signal with a square wave reference of the same frequency and filtering the product.

When the a.c. and the reference signals are in phase and of the same frequency, the output of the psd is a d.c. voltage proportional to the RMS voltage of the a.c. input. A phase difference θ between the signal and the reference inputs leads to an output

$$V_{\text{output}} = AV_{\text{input}} \cos\theta \tag{3.1}$$

where A is a constant. If the frequencies of the signal and reference inputs are different, the output of the psd is an a.c. signal. This signal consists of sum and difference frequencies of the signal and reference which average to zero if the time constant of the low pass filter is sufficiently high.

The choice of the reference frequency is very important since a square wave is composed of sine waves at the fundamental frequency and its odd harmonics given by

$$V_R(t) = V_R \sum_{n=0}^{N} \frac{1}{2n+1} \sin[(2n+1)\omega_R t] \tag{3.2}$$

which could correspond with strong interference signals. To overcome this problem one has to avoid very low frequencies. Frequencies that are multiples of 50 Hz are also bad choice since one can get unwanted information generated by harmonics from the mains.

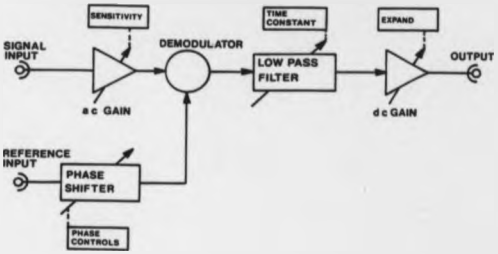

Fig. 3.1. A simplified block diagram of a pad (Brookdeal 9503).

3.2.3 The Experimental Apparatus

A schematic representation of the apparatus is shown in Fig. 3.2. In describing the apparatus it is convenient to consider the optical and electronic parts separately.

3.2.3.1. The Optical System

The light source was a 150 Watt Xe lamp (XBO). The lamp was mounted in steel lamphouse (Ealing). The lamp was supported from its top on the front panel assembly of the lamphouse which also provides external adjustments for both centering and focusing. The lamphouse was also fitted with a 35 mm aperture U. V. grade fused silica condenser. A vibration free fan was fitted at the bottom of the lamphouse to keep the lamp terminals cool while maintaining the envelope warm. This cooling system was designed to ensure that the arc operates at its maximum efficiency throughout the life time of the lamp. The lamp was powered with a universal ARC lamp supply 250 Watt (Ealing) which gave a high stability d.c. output.

The light beam coming from the Xe arc lamp was focused, using a fused silica lens, onto the entrance slits of the grating monochromator (Bausch and Lomb) fitted with a U. V. grating (1200 Grooves/mm) giving monochromatic light of a wave length in the range of 200 to 700 mm. The entrance and exit slits were adjustable. A maximum throughput was achieved by adjusting the entrance slits so that the image of the arc could just fill them. The exit slits were also adjusted to give a band pass of 1.5 nm. The monochromator was driven by a computer controlled stepper motor system which had a resolution of 0.15° (equivalent to 0.33 nm).

The monochromator beam was chopped with a light chopper (Brookdeal 9479), fitted with a three slot chopping blade in order to give a frequency range of 0.5 Hz to 100 Hz. The light chopper provided a square wave output of the same frequency as the chopped light which was used as the reference signal input for the phase sensitive detector.

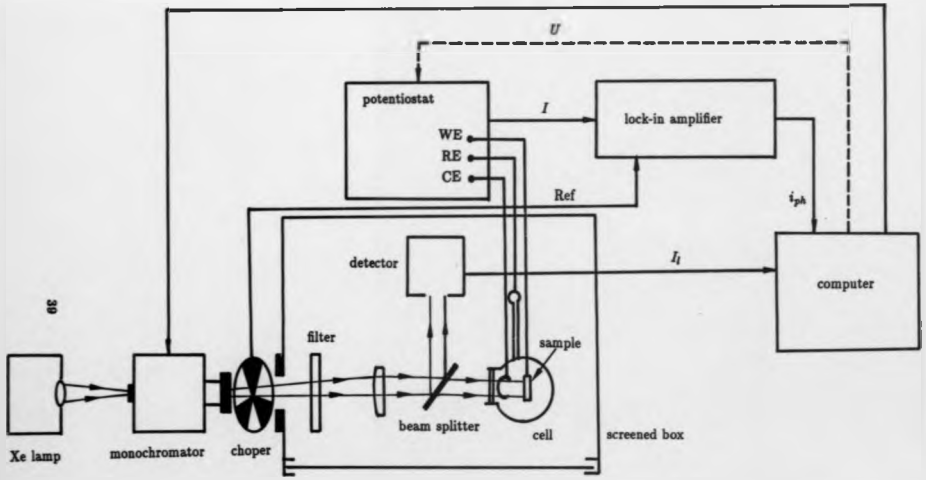

Fig. 3. 2. A schematic representation of an experimental set up for photoelectrochemical studies of passive films.

Where appropriate higher order diffracted beams in the chopped monochromatic light were filtered out with a band pass filter transmitting in the range of 300 to 600 nm. The beam was then collimated with a fused quarts plano-convex lens and split into two components with a fused quarts beam splitter. 80% of the beam was used to illuminate the sample, in the cell, and the remaining 20% was used to measure I_0.

I_0 was measured using a photodiode detector which consisted of a 1 cm^2 pin silicon photodiode, having a wave length range of 300 to 1050 nm, and low noise FET operational amplifier. When illuminated the photodiode generated a current which flowed through the operational amplifier feedback resistor and generated a d.c. output voltage. The gain was controlled by the feedback resistor (10 kΩ - 1 MΩ) giving rise times for the combination of 10 μs to 100 μs. The electronic components were mounted on a stripboard which was housed in an alloy cast box to prevent pick-up. The circuit was powered by $\pm$ 15 V outputs from a EuroBEEB single board computer with AD and DA converter. The same computer was also used to measure the output of the photodiode detector.

The optical components were mounted on two optical benches. The lamp, the monochromator and the light chopper were mounted on a flat optical bench which was mounted on a heavy wooden base. The rest of the components were mounted on a triangular optical bench by means of adjustable mounts. In order to avoid pick-up and to exclude ambient light the triangular optical bench was housed in an earthed light proof metallic box. This box had its interior painted in black, to absorb any incident light, and was mounted on another separate heavy wooden base to avoid any vibration which may come from the light chopper. The box also sat on rubber bungs to damp vibrations. The photodiode detector was also enclosed in this box.

3.2.3.2. The Electrochemical Control Equipment

The electrochemical experiments were performed in a three electrode system with all potentials measured with respect to a saturated calomel electrode (SCE). The working electrode potential was controlled by using a potentiostat type DT 2101 (Hi-tek Instruments) in conjunction with a wave form generator PP R1 (Hi-tek Instruments) and slow sweep voltamograms were recorded on an X-Y recorder (type PL4, J J Instruments). In the photocurrent spectroscopy experiment, however, the potential of the working electrode was controlled by means of a ministat E-series (Thompson Electrochem Ltd) controlled by a EuroBEEB single board computer with A/D and D/A converters.

3.2.3.3. Data Acquisition of the Photocurrent

As described earlier the electrode was illuminated with a chopped, monochromator light beam. The resulting current from the cell was the sum of the d.c. polarisation current and the a.c. current generated by the alternating illumination of the working electrode (photocurrent) which was very small. The cell current was fed to the signal channel of the pad and the reference signal was supplied by the chopper. The pad used in this work was a lock-in amplifier (LIA) (Brookdeal 9503) which had a frequency range of 1 Hz to 50 kHz. The incorporation of the calibrated phase shifter in the reference signal channel of the LIA made compensation for phase shifts in the electrochemical equipment possible. The output of the LIA was a d.c. voltage proportional to the photocurrent, generated by illumination of the working electrode. This voltage was fed to the computer controlling the experiment (EuroBEEB) via an A/D converter. The details of the data acquisition are given later in section 3.1.6.

3.2.3.4. The Electrochemical Cells and Electrodes

Two cells were used to carry out the electrochemical experiments. One was used for the polarisation studies and the other was for the photocurrent spectroscopy studies. Fig. 3.3 shows a schematic representation of the cell used for the polarisation experiments. It was made from a pyrex beaker. The PTFE lid supported the working electrode and the two pyrex compartments with fritted glass bottoms where the secondary and reference electrodes were positioned. These compartments were used to avoid chloride ions (Cl^-) from the SCE or oxygen generated by the secondary electrode reaching the working electrode. The other cell, shown in Fig. 3.4, was made of PTFE. It was cylindrical in shape and had a fused silica optical quality window through which light could pass. The cell had two compartments, one for the working and the secondary platinum electrodes. The other compartment was made of pyrex glass linked to the first one by a pyrex pipe (Luggin capillary) going close to the working electrode. This compartment was used to accommodate a reference electrode after it had been put in a pyrex tube with frit glass bottom on which an Agar-Agar gel had set. This gel was used to prevent Cl^- ions from the SCE getting into the solution in the compartment where the sample was sited. The lid of this cell was used to support the working electrode and the secondary electrode, shaped as a ring to avoid interference with the light beam. An extra hole was drilled in the lid to let gases escape.

Since the aim of this work was to study the effect of chromium content on the structure of the passivated films that form on Iron/Chromium alloys, a series of electrodes was made with the chromium content varying from 0-25 atomic per cent. According to the experiment the material used in these studies was prepared in different ways. The samples were prepared either as bulk Iron and Iron/Chromium alloys (from British Steel) or as thin films of Iron and Iron/Chromium alloys. The bulk samples were prepared as electrodes from 1 cm × 1 cm × 0.2 cm pieces of either pure Iron or Iron/Chromium alloys (Fe 5, 10, 15,

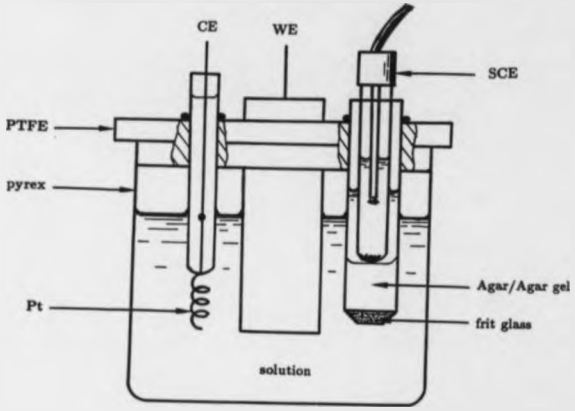

Fig. 3. 3. A schematic representation of the cell used for the polarisation experiments.

Fig. 3. 4. The electrochemical cell used for the photoelectrochemical experiments.

20 and 25 atomic% Cr). Each piece was attached on one side to a copper wire by using a conducting silver epoxy resin to ensure an electric contact. The electrodes were then sealed in cylindrically shaped epoxy resin moulds which were mounted on glass slides using epoxy resin. The other side of each electrode was abraded so as only a flat 1 cm^2 face was exposed. Thin films ($\sim$ 100 $\AA$) of both Iron and Iron/Chromium alloys were prepared by vapour deposition from tungsten filaments in a good vacuum either directly onto cleaned mylar or more frequently onto mylar on which a 200 $\AA$ layer of gold had previously been deposited. The gold substrate was used to ensure a good electrical contact since the metallic film under investigation becomes semiconducting after anodisation, therefore the material becomes more resistive. The composition of the films were checked, after deposition, by X-ray analysis with a transmission electon microscope.

3.2.4 Preparation of the Solutions and Glassware

The water used to prepare all solutions was prepared with deionised water that had been further purified by slow distillation. This water was stored in a 10 l pyrex container with ground glass stopper. All solutions were prepared and stored in 1 l pyrex volumetric flasks with nylon tops.

All glassware and the cells were cleaned by prolonged immersion an a mixture of deionised water and Decon90 then rinsed thoroughly with deionised water and a final rinsing with distilled water.

3.2.5 Electrode Preparation

The bulk electrodes were abraded with progressively finer grades of silicon carbide paper and finally a dry finish with 4/0 emery paper. Then the electrodes were wiped with dry soft clean tissue and transferred immediately to the cell which was filled with deoxygenated solution.

The electrodes were not rinsed to avoid reaction of the electrode surface with the dissolved oxygen in water. The reason that the electrodes were left abraded was to increase the surface area in the photocurrent experiment. The effective surface area of the film electrodes could not be increased in this way and therefore these electrodes were transferred directly from the vacuum chamber to the cell filled with deoxygenated solution.

3.2.6 Experimental Procedure

3.2.6.1 Polarisation Measurements

When the electrode was prepared and the cell was filled with deoxygenated solution, the electrode was cathodically polarised in the hydrogen evolution region for 30 minutes to clean off the oxide inevitably formed after exposure to air. Then a slow voltage sweep (0.5 mV/s) was applied and a polarization curve ($i = f(U)$) was recorded on the X-Y recorder.

3.2.6.2 Photocurrent Measurements

Two different experiments were performed for the photocurrent spectroscopy namely the determination of the wave length and potential dependence. Both required exactly the same surface film preparation. The electrode was cathodically treated as mentioned above and then the potential was stepped to a chosen anodic potential for 30 minutes to form the oxide film before any optical measurement.

a. Wave Length Dependence of the Photocurrent

Once the oxide had been formed at a chosen potential, the cell was aligned correctly in the light beam. Then the dark box was closed to avoid any interference from ambient light and the experiment was ready to be started. The potential was set to a value which gave a large signal i.e. 0.7 V in the case of the borate solution which had pH of 8.4. As the oxide

was stable this value was chosen regardless of the potential of its formation. By using the EuroBEEB computer the monochromator was set to give monochromatic light with a wave length of 600 nm. Then five (5) seconds later the sampling procedure started. In the case of electrodes with chromium content lower than ten atomic per cent (10 at.%), the output of the LIA was sampled at rate of 10 samples per second. Twenty readings were then taken and averaged to give one value of the photocurrent (I_{ph}) for a given wave length. However, once the chromium content exceeded ten per cent, 200 samples were needed to get a reliable reading. This was due to the reduction of the signal believed to be caused by the presence of a substantial amount of chromium(III) hydroxide, known to be a good insulating material, in the passive film formed on electrodes of this composition. The incident light intensity (I_0) was also sampled. The sampling rate was 1000 samples per second and 200 readings were obtained in 0.2 of a second. However, only selected regions of the signal were considered since the photodiode detector was detecting a chopped light which gave a square wave output. Therefore only high values within 95% of the maximum were kept and averaged to give the value representative of I_0. As the light beam detected by the photodiode was 20% of the total incident beam, the photocurrent was corrected for the lamp emission by dividing it by $I_l = 4I_0$. When the first data point, (λ_1, $I_{ph1}/4I_{01}$) with λ = 600 nm, was plotted on the screen and stored on floppy disc then the monochromator was moved to a wave length of 595 nm. The sampling procedure was delayed by 5 seconds to allow the stabilization of the photocurrent after which a second data point was obtained by the same procedure. The sequence was then repeated by decreasing the wave length by a step width of 5 nm till a range of 600 nm to 300 nm was covered. Finally the disc file was closed and the data was transferred to a mainframe computer for further processing.

b. Potential Dependence of the Photocurrent

A similar procedure as described above was used to determine the potential dependence of the photocurrent, except that the photocurrent was in this case measured at a constant wave length whilst sweeping the voltage.

A wave length of 380 nm was chosen in all measurements of the potential dependence of the photocurrent experiment as this wave length gave a large signal. When the experiment was ready to be started the working electrode voltage was set to a value below the flat band potential according to the pH of the solution used. This potential was situated somewhere in the passive region on the polarisation curve in order to prevent the reduction of the oxide under investigation. The sampling procedure was delayed by one minute to allow the photocurrent to stabilise. This time delay was 15 times longer than in the case of the wave length dependence experiment due to the instability of the photocurrent as a result of the surface state change when the applied voltage was varied. The first data point (U_1, I_{ph1}) was measured by using the same procedure as stated in the wave length dependence of the photocurrent section. The polarization current (I_p) was also measured at the same time to check the electrochemical behaviour of the working electrode during the experiment. When the two data points, (U_1, I_{ph1}) and (U_1, I_{p1}), were plotted on the screen and stored on floppy disc the potential of the working electrode was stepped to $U_2 = U_1 + 0.015$ Volt. One minute later two other data points were measured. The sequence was repeated by increasing the voltage by a step width of 0.015 Volt till the oxygen evolution region was reached. The data were then transferred to the mainframe computer for further processing. In this experiment both the forward and reverse voltage sweeps were performed on the same surface oxide film and the data showed essentially no differences.

3.3 X-ray Absorption Spectroscopy Experiment

3.3.1 Introduction

This part of the chapter is concerned with the experimental apparatus used for an X-ray absorption measurement, the description of the electrochemical cell and the sample preparation. The experimental procedure is also described.

3.3.2 The Experimental Apparatus

The EXAFS experiments were carried out by using the Synchrotron Radiation Source (SRS) storage ring at Daresbury Laboratory. The experimental arrangement is illustrated in Fig.3.5. As in the case of the photocurrent work the experimental apparatus is described below by considering the optical and electronic parts separataly.

3.3.2.1. The Optical System

The radiation emitted by the storage ring was filtered by using a beryllium (Be) window, 265 μm thick, placed just before the monochromator in order to remove the visible and the ultra-violet light.

The filtered X-ray beam was then monochromated by a double crystal monochromator. The crystals were Si(111) crystals which cover the wave length range of 1.5 $\AA$ to 4 $\AA$. This made measurement of EXAFS above Fe and Cr K-absorption edges, which are 1.9 $\AA$ and 2.2 $\AA$ respectively, possible. To correct for the vertical divergence of the X-ray beam the crystals were pre-bent to a radius of 55 m in the diffraction plane. The first crystal of the monochromator was fixed with respect to the horisontal plane and was water cooled, The second crystal, however, when moved to another energy position was translated in the horisontal plane to keep the monochromator beam at the same height. This crystal was also detunable to reject harmonics and was not cooled since only monochromatic light was falling

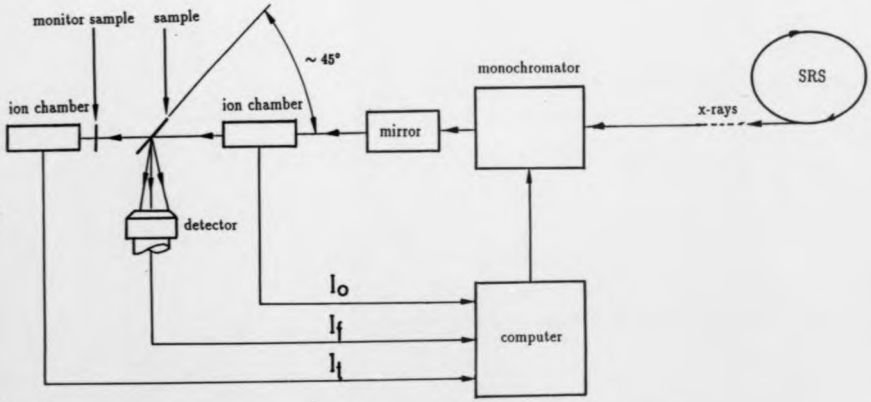

Fig. 2. 5. A schematic representation of the experimental configuration for recording an EXAFS spectrum.

on it.

The monochromatic beam was also filtered with a 62.5 μm Be window located at the far side of the monochromator vessel. The beam was reflected off a post-focusing mirror and finally passed through a 250 μm Be window valve immediately before the sample area.

The monochromator and the platinum mirror were enclosed in a high vacuum vessel, about 4×10^{-7} torr, and the rest of the line was pumped down to pressures of 10^{-8} torr or better[60].

The focused monochromatic beam passed through a stainless steel ion chamber with two Be windows. This ion chamber absorbed 20% of the beam and its output represented the incident intensity I_0. The remaining 80% of the monochromatic beam was used to illuminate the sample.

In the transmission EXAFS mode a second ion chamber was placed immediately after the sample positioned on a perspex frame which was mounted on an adjustable mount. This ion chamber absorbed the transmitted beam and the intensity I_t was measured. Both ion chambers used the same 300 Volt power supply. These ion chambers, the sample mount as well as a laser, used to align the sample in the beam, were mounted on an optical bench. The optical bench was mounted on a heavy metal table.

The fluorescence samples were positioned either on a perspex frame or on the window of an electrochemical cell described later. The frame or the cell were mounted on the optical bench by means of an X-Y-Z mount. The fluorescence radiation was measured with either a scintillation detector or with an array of solid-state detectors.

3.3.2.2. The Fluorescence EXAFS Detection

For dilute systems, fluorescence mode is more sensitive than transmission mode. Fluorescence EXAFS detection has improved since the first measurement by Jaklevic et al in 1977 [61] using

a single solid-state Ge-Li detector. The count rate capability of this detection system has been exceeded by the increased intensity from current focused beam lines. This has led to the use of an array of NaI scintillation detectors[62] but the fluorescence signal remains obscured by scattered X-ray radiation for dilute systems. To discriminate against this background while maintaining a large angular acceptance and high count rate, a new detection unit has been constructed[63]. This unit designed by Cramer et al was based on an array of solid-state Ge detectors.

Fig. 3. 6 shows the front of the fluorescence detection unit which was based on an array of 13 solid-state Ge detectors arranged in star-shaped pattern in a common liquid nitrogen cryostat. Each individual Ge detector was a 10 mm thick planar slice 11.3 mm in diameter and was connected to a discriminator for windowing the amplifier output.

In this work only a combination of 8 Ge solid-state detectors was used. Having a good solid angle acceptance, this fluorescence detection system gave good background rejection at a high count rate as well as good electronic stability. The individual count rates were set to a maximum limit of 10^4 counts/s in order to avoid pile-up. This was achieved, if necessary, by detuning the monochromator slightly.

3. 3. 2. 3. Fluorescence EXAFS Data Collection

The absorption spectra using fluorescence EXAFS mode have been obtained by means of fluorescence detectors. The sample was located at about 10 cm from the first ion chamber which was lead shielded, to prevent any fluorescence from steel, and about 7 cm from the front of the detector. The sample was positioned, as already mentioned in the previous section, on either a perspex frame or on the mylar window of an electrochemical cell so as to make an angle of about 45° with the incident beam as shown in Fig. 3. 5. In this work two types of fluorescence detectors were used; a single scintillation detector[62] and an array of solid-state

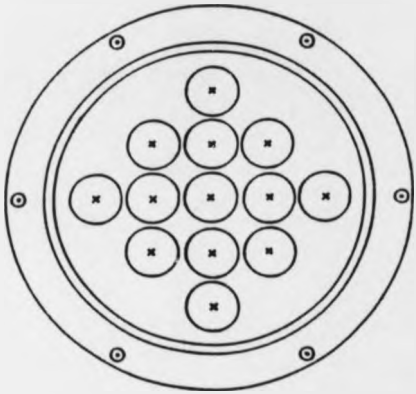

Fig. 3. 6. A schematic diagram of the front of the fluorescence detection unit used in this work. The circles represent the individual Ge solid state detectors.

detectors[63]. In the case of the scintillation detector scattered radiation affected badly the signal to background ratio. This effect was reduced by placing a 15 μm thick MnO_2 filter immediately at the front of the detector. However, better results were obtained with the solid-state detectors without any filtering. The data collection with either detector system was achieved by feeding the output of each detector to a single channel analyser and the output of each of these analysers was recorded as was I_0 on a disc of the LSI 11 computer. The sum of all detectors normalised to I_0 was displayed, in real time, on the screen. The computer was also used to control the monochromator.

3.3.2.4. The Electrochemical Cell and Samples

Two cells were used. The first cell, shown in Fig. 3.7 consisted of a perspex reservoir connected to a glass compartment with a glass tube. The glass compartment served to accommodate a SCE which was isolated in another glass tube with a fritted glass bottom on which an Agar-Agar gel had set. At the bottom of the reservoir lay a platinum gauge used as a secondary electrode. The working electrode was a thin iron or iron/chromium film deposited on a gold film on mylar flag. This flag was supported by a sample holder which could slide up and down on two front posts. These ports also supported a thin mylar window where the working electrode was mounted after the electrochemical treatment for an X-ray absorption measurement. capillary attraction ensured that the electrode remained wet throughout the experiment. This cell was also used in the in-situ fluorescence EXAFS measurements from the samples passivated by simple immersion into the solution. In this case the cell was simply disconnected.

The second cell shown in Fig. 3.8 also consisted of a perspex reservoir connected to a glass compartment, where a SCE was accommodated, with a glass tube. However, this cell has the advantage of keeping the sample in the same position throughout the whole experiment, hence

Fig. 3. 7. A cell used in the *in-situ* EXAFS experiments to study films passivated both electrochemically and by immersion into the solution.

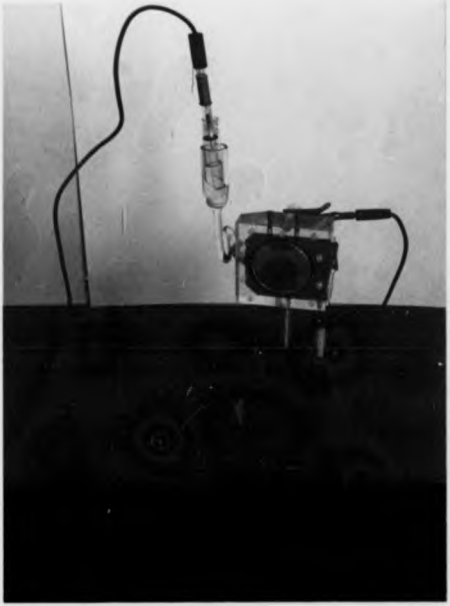

Fig. 3. 8. An alternative electrochemical cell used here in the *in-situ* EXAFS studies of the passive film.

the working electrode remains facing the secondary Pt one even during the X-ray absorption measurements. This was rather convenient since the electrochemical conditions were kept constant. The working electrode was also used as a window, which was fixed to the front of the cell with a perspex frame tightened with plastic screws. The cell can be filled from one of the two holes drilled in the top which were then blocked with rubber bungs to prevent oxygenation of the solution during the experiment.

The fluorescence samples were films of either pure iron or iron/chromium alloys made in the same way as explained in the photocurrent experiment. However, the thickness of these films was approximately 20 $\AA$. The choice of this thickness was made to ensure full conversion of the metallic film to passive film material, since the sampling depth of the fluorescence EXAFS in the K-absorption edges of both Fe and Cr is as large as 500 $\AA$ and the passive film formed on iron does not exceed 30 $\AA$. The fluorescence samples also include two films of FeOOH electrodeposited on mylar coated with a 200 $\AA$ thick layer of gold.

The transmission samples used as model compounds were commercially produced powders of α-Fe_2O_3, γ-Fe_2O_3, α-FeOOH, γ-FeOOH, α-Cr_2O_3, $Cr(OH)_3$, K_2CrO_4 and $K_2Cr_2O_7$.

3.3.3 The Sample Preparation

The fluorescence samples were divided into two groups. The films passivated by simple immersion in the solution and the ones prepared under potential control. Pure iron and iron/chromium alloys made as films deposited directly on cleaned mylar were passivated by simple immersion in 0.01M sodium nitrite ($NaNO_2$) and 0.005M potassium chromate (K_2CrO_4). The choice of these solutions was based on the knowledge that they are moderately good passivating solutions and the passive films formed in these solutions seem to be similar to those formed electrochemically in solutions free from ferrous ions[84]. After three weeks of passivation the samples were transferred to the cell for an *in-situ* X-ray absorption

measurement. Fe, Fe15%Cr and Fe25%Cr samples, passivated in both solutions, were selected for *ex-situ* EXAFS studies as a comparison with the *in-situ* ones since this range covers the transitions in passivating quality which have been reported to occur at chromium contents of 15 and 25 per cent[65]. These films were washed in distilled water and dried with clean nitrogen (N_2) then put in a vacuum (10^{-3} torr) for 36 hours prior to the EXAFS measurement. As far as the *in-situ* potentiostatically controlled EXAFS experiment is concerned the material was iron and iron/chromium alloys films on 200 $\AA$ thick films of gold (Au) deposited on cleaned mylar as explained earlier. In addition to its good electric conductivity the gold substrate was chosen here because its L- and K-absorption edges are far from the iron K-absorption edge. The gold was exposed to the solution and there was gold oxide formation but this did not interfere with the experiment. The sample coming from the vacuum chamber was transferred to the electrochemical cell which was then filled with a deoxygenated solution. The sample was positioned so as to float on the surface of the solution facing the secondary electrode. The working electrode was then cathodically treated in the hydrogen (H_2) evolution region for 30 min then converted to an oxide by stepping the voltage to the required anodic value. When the anodic current stopped decreasing the working electrode was taken to the mylar window of the cell by sliding up the sample holder whilst maintaining potentiostatic control. The lower part of the sample was floating on the surface of the solution. The experiment was then ready to be started. The electrochemical equipment used here was the same one used to carry out the photocurrent experiment. In the case of the second cell (Fig. 3. 8) the sample was held at the same position throughout the whole experiment. This had the advantage of keeping exactly the same electrochemical conditions during the experiment. The other advantage of this cell was its easy flushing under nitrogen atmosphere after the cathodic treatment.

The two FeOOH films were anodically deposited on mylar coated with 200 $\AA$ thick gold

layer at 0.3 V from 0.15M $(NH_4)_2SO_4$ + 2 × 10^{-4} Fe^{2+} and borate buffer (pH 8.4) + 2 × 10^{-4} Fe^{2+} solutions[66,67] for an hour. The films were removed from the solutions, washed in distilled water and dried with clean nitrogen after which they were taken for an *ex-situ* fluorescence EXAFS examination.

The eight model compounds, mentioned in the previous section, were prepared by grinding the commercial powders in amyl-acetate using an agate mortar. When the grains looked even in size durofix resin was added and mixed with the powder and amyl-acetate. The product was then cast in a mould prepared using a microscope slide covered with a sellotape and along either of the largest sides of the microscope slide, two super-imposed PVC tape pieces were stuck to give reasonably thick samples. When the mould was ready the mixture of powder, amyl-acetate and durofix was cast into it then leveled with a microscope slide. After drying this in air, a manageable film was obtained which was stripped off the sellotape[68].

3.3.4 Experimental Procedure

3.3.4.1. Fluorescence EXAFS Measurements

When the sample was prepared and aligned properly in the beam the experiment was ready to be started. The calibrated monochromator was set to scan through three regions, the pre-edge, near edge and EXAFS regions. In the case of an angle scan, the energy resolution was chosen to be different for all regions and was determined with respect to the importance of the region. In the case of a k-space scan, however, these regions were used to calculate new regions to give evenly spaced data points with an EXAFS region not exceeding 200 points since this was the maximum limit that could be used to run the EXCURVE package[56]. The monochromator was taken to the beginning of the scan and the experiment was started by measuring the first data point ($\frac{I_{f1}}{I_{o1}}$, E_1). The point was displayed in real time and stored on a disc of the LSI 11 computer. The monochromator was moved to another energy position

E_2 and a second point ($\frac{I_f}{I_{o2}}$, E_2) was obtained and the procedure was repeated for all energy positions of the monochromator required to cover the three regions of the scan. When a scan was complete the file was closed and the monochromator was reset to the beginning of the scan. Depending on the quality of the data a number n of scans was chosen for each sample to be averaged together to improve the signal to noise ratio by a factor of $\sqrt{n}$. At the end of the experiment data files were transferred from the LSI 11 computer to the main frame computer for further processing.

The energy calibration was monitored by measuring a transmission spectrum from a foil located behind the transmission cell (generally the fluorescence samples were too thin to absorb a significant amount of radiation and hence the presence of this material does not significantly affect the transmission spectra).

3.3.4.2. Transmission EXAFS Measurements

The same procedure as above was used to measure X-ray absorption spectra in the transmission mode except that the transmitted beam intensity I_t was measured by using an ion chamber. In this mode the data was $f(E) = l_n \frac{I_t}{I_o}$.

Chapter 4

Electrochemical and Photoelectrochemical Behaviour of Iron and Iron/Chromium Alloys

4.1 Introduction

Polarization curves and photocurrent spectroscopy have been used to characterise the passive film on iron and iron/chromium alloys prepared as bulk or thin films. To this end, it is convenient to present the results for the two types of material separately.

4.2 Results and Discussion of the Electrochemical and Photoelectrochemical Studies of Bulk Iron and Iron/chromium Alloys

4.2.1 Electrochemical Behaviour

Fig. 4. 1 presents polarisation curves for pure iron and various iron/chromium alloys. These curves were obtained in a borate buffer solution (pH 8.4) by sweeping the voltage from −0.8 to 1.0 V at a rate of 0.5 mV/s. Curves (1) and (2) were obtained for pure iron and 5% chromium alloy. They show no significant differences except that the current density is lower in the case of 5% chromium alloy. As the chromium content increases the current density decreases and

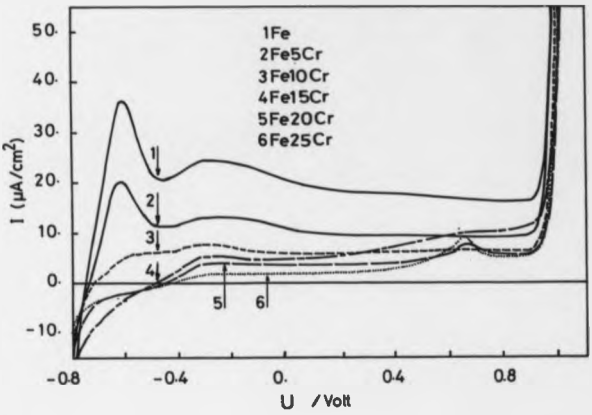

Fig. 4. 1. Polarisation curves in borate buffer solution for bulk Fe and various Fe/Cr alloys.

features present in curves (1) and (2) disappear whilst another feature appears just before the oxygen evolution potential. The same feature has been observed for these alloys passivated in 10% sulphuric acid[3] and this was identified as a transpassive region where it was believed that the film was thickening. This idea is supported in the next section where photocurrents for high chromium content alloys were only detectable at voltages higher than +0.9 V. For alloys of chromium content higher than 10%, the hydrogen evolution region is shifted from −0.75 to −0.55 V due to the chromium catalysing the process. The passive region for Fe, Fe5%Cr and Fe10%Cr samples spans from −0.4 to 0.9 V whereas for higher chromium content alloys this region is reduced to −0.4 to +0.4 V but there is additionally the transpassive one. It should also be noted that Fig. 4.1 indicates that there is a decrease in the passive current as chromium content increases.

4.2.2 The Energy Dependence of the Photocurrent Spectroscopy Data

Spectra shown in Fig. 4.2 are those for iron and various iron/chromium alloys. These spectra show that the magnitude of the photocurrent decreases as chromium content increases. There are two possible explanations for this behaviour, one is that the passive layer formed on Fe/Cr alloys is thinner for high chromium content or, alternatively, the passive film on high chromium alloys contains less iron oxide or iron in a different form. In this work the photocurrent generated from passivated pure chromium was very low and not easy to detect as it was completely obscured by the noise. Therefore it is fairly obvious that the photocurrents from passive layers formed on high chromium alloys are expected to be small since only a small amount of iron is present in these films.

The passive films formed on Fe and Fe/Cr alloys were assumed to be n-type semiconductors with indirect allowed transitions[20,27]. Therefore the data were processed to give the $((I_{ph}/I_l).h\nu)^{1/2}$ vs. $h\nu$ plots presented in Fig. 4.3. Up to 10% Cr content these plots were fitted to straight lines and when extrapolated to $I_{ph} = 0$ they yielded the band gap ener-

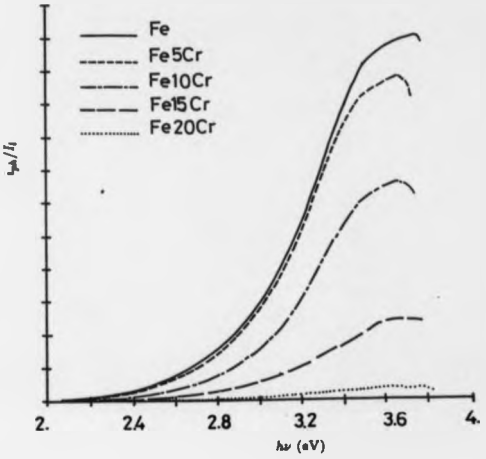

Fig. 4. 2. Energy dependence of the photocurrent spectra, normalised to the lamp emission, for the bulk samples passivated at + 0.9 V in borate buffer solution.

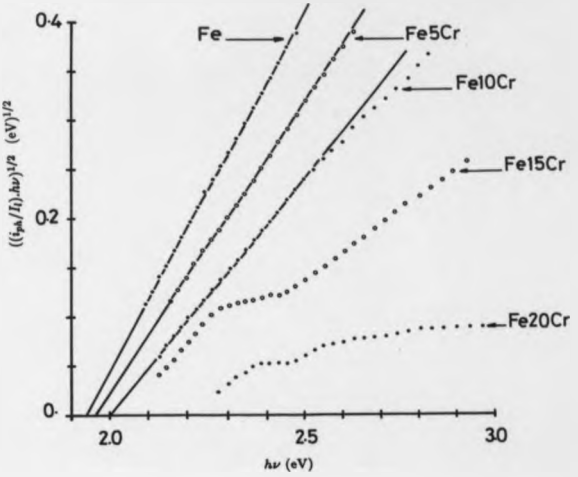

Fig. 4. 3. $((i_{pa}/I_l).h\nu)^{1/2}$ vs. $h\nu$ plots for the bulk samples passivated at + 0.9 V in borate buffer.

gies shown in Table 4.1. Above this composition the data become difficult to analyse. Of particular interest are the data obtained for Fe15%Cr alloy which can be fitted with two straight lines of different slopes. This bilinear fitting may be explained by the presence of two simultaneous phases in the passive film formed on Fe/Cr alloys. By referring to Fig. 4.2 it can be seen that there is an effective increase in the band gap energy towards that of the passive film formed on pure chromium, which has been found to be 2.5 eV[22], as the chromium content increases. This suggests that the passive layer on Fe/Cr alloys could be a mixture of oxide phases of iron and chromium.

Fig. 4.4 shows $((I_{ph}/I_l).h\nu)^{1/2}$ vs. $h\nu$ plots for Fe15%Cr passivated at different anodic potentials. These curves yield a decreasing band gap energy as the potential at which the passive film is formed increases. This suggests that passive films formed on iron-chromium alloys at low anodic potentials are rich in chromium whereas those formed at high potentials consist mainly of 'iron oxide'. This conclusion is in agreement with Okamoto's work[68] on 18/8 stainless steel. The optical band gap energies for iron and iron/chromium alloys passivated at various anodic potentials in borate buffer solution (pH 8.4) are listed in Table 4.1. In the case of Fe20%Cr alloy the only analysable photocurrent spectra are those obtained after passivation at anodic potentials greater than 0.9 V and in the case of Fe25%Cr sample an anodic potential of 1.2 V was needed to obtain a detectable photocurrent. Therefore it can be deduced that the presence of high quantities of chromium in the alloy prevent the formation of iron oxide[1]. This is largely as expected as Cr will oxidise more readily than Fe to form what appears to be a good passive layer. The iron oxide seems to form only at high potentials probably after breaking the passive chromium layer in the oxygen evolution region. An alternative explanation is that perhaps all the iron was dissolved away during the sample cleaning at cathodic potentials and therefore only chromium metal was left at the surface which led to the protection of the underlaying metal at low anodic potentials. This

	U/volt (SCE)				
	0.7	0.8	0.9	1.0	1.2
Fe	1.96	1.96	1.91	2.12	
Fe5%Cr	2.00	1.90	1.95	2.00	
Fe10%Cr	2.17	2.00	2.00	1.96	
Fe15%Cr	2.4	1.90/2.04	2.00/2.00	1.90/1.90	
Fe20%Cr			2.22	2.17	
Fe25%Cr					2.20
	E_g^*/eV ($\Delta E_g^* = \pm$ 0.01 eV)				

Table 4.1. Apparent optical band gaps of bulk iron and iron/chromium alloys passivated in borate buffer solution at various voltages.

	U_{fb}/volt ($\Delta U_{fb} = \pm$ 0.05 V)				
pH	Fe	Fe5%Cr	Fe10%Cr	Fe15%Cr	Fe20%Cr
8.4	0.00	0.00	-0.14	-0.14	-0.14
13.0	-0.12	-0.12	-0.27	-0.27	

Table 4.2. Flat band potentials of bulk iron and iron/chromium alloys passivated at + 0.9 V in borate buffer (pH 8.4) and 0.1 M NaOH (pH 13) solutions.

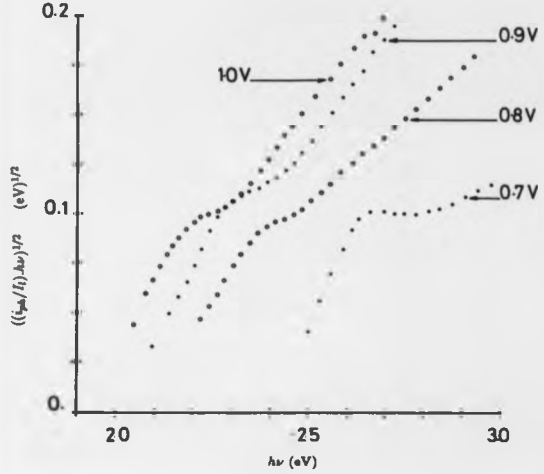

Fig. 4. 4. $((i_{ph}/I_i).h\nu)^{1/2}$ vs. $h\nu$ plots for bulk Fe15%Cr alloy passivated at different potentials in borate buffer solution.

explanation is however unlikely.

4.2.3 The Potential Dependence of the Photocurrent Data

The potential dependence of the photocurrent spectra for iron and various iron/chromium alloys were recorded in either borate buffer (pH 8.4) or in 0.1M NaOH (pH 13) solutions. By using these data it was not easy to determine accurately the flat band potential as the data were noisy at low potentials. The values obtained for the flat band potentials (Table 4.2) are higher than those obtained from capacity measurements[26,37,48] by several hundred millivolts. However, the line shape and position of the peak of the I_{ph} vs. U plots as well as the magnitude of the photocurrent can yield information about the nature of the passive film on iron/chromium alloys.

Fig. 4.5 presents I_{ph} vs. U plots for iron and various iron/chromium alloys passivated at 0.9 V in borate buffer solution. The photocurrent generated from the iron sample peaks at 0.78 V and as the chromium content in the alloys increases this peak is shifted slightly towards lower values of U. The peak broadens as the chromium content increases and in the case of Fe15%Cr alloy the I_{ph} vs. U plot is asymmetric, a shoulder having developed on the low voltage side. As the alloy becomes richer in chromium, there is also an increase in the effective flat band potential towards negative values and a decrease of the photocurrent magnitude. The essential invariance of the peak position in the I_{ph} vs. U plots with changing alloy composition can be attributed to the formation of the same 'iron oxide' phase in the passive layer on all alloys regardless of the composition whereas the variation of the flat band potential, the broadening and the asymmetry of the I_{ph} vs. U plots can be explained by the presence of chromium oxides in the passive layer. As already mentioned in the previous section the decrease of the photocurrent magnitude with the increase of chromium content may be due to the decreasing thickness of the passive layer or to the reduction of the quantity of iron in the passive film.

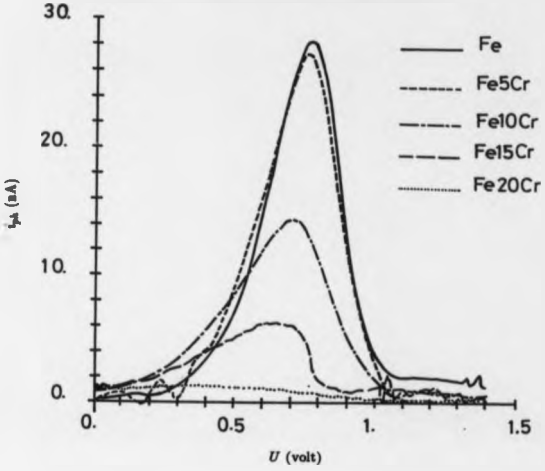

Fig. 4. 5. Potential dependence of the photocurrent spectra for the bulk samples passivated at + 0.9 V in borate buffer solution.

The same behaviour is observed for samples passivated in 0.1M NaOH (pH 13) and the results are presented in Fig. 4.6. In this figure the spectral features are displaced by −0.35 V with respect to those obtained for samples passivated in the borate buffer solution. This is due to the change in the nature of the solution from pH 8.4 to pH 13.

4.3 Results and Discussion of the Iron and Iron/Chromium Alloys Prepared as Films

4.3.1 Electrochemical Behaviour

The polarisation curves for pure iron and iron/chromium alloys, prepared as thin films on mylar, were obtained by sweeping the potential from −0.7 to 1.0 V at a rate of 0.5 mV/s. These curves are presented in Fig. 4.7 and should be compared with Fig. 4.1 for bulk materials. The curves are essentially the same except that the current densities are lower for the films, presumably because of the lower surface roughness, and the small peak seen at 0.6 V for the bulk materials with high chromium content is less well defined for the films. On the basis of these data it can be concluded that the films appear to behave in a similar way to the bulk materials.

4.3.2 The Energy Dependence of the Photocurrent

The dependence of the photocurrent on photon energy for pure iron and iron/chromium alloys prepared as films on mylar is illustrated in Fig. 4.8. These films were passivated at 0.9 V in the borate buffer solution (pH 8.4). As expected the magnitude of the photocurrent decreases as the chromium content increases. This was also observed for the bulk material, but the decrease in the magnitude of the photocurrent was approximately linear with composition whereas in the case of film electrodes there is a slight decrease from pure Fe and Fe5%Cr samples and then a large drop between Fe5%Cr and Fe10%Cr alloys after which the photocurrent

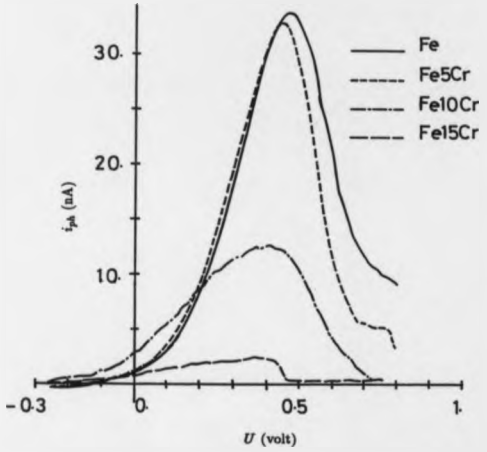

Fig. 4. 8. Potential dependence of the photocurrent spectra for the bulk samples passivated at + 0.9 V in sodium hydroxide solution (pH 13).

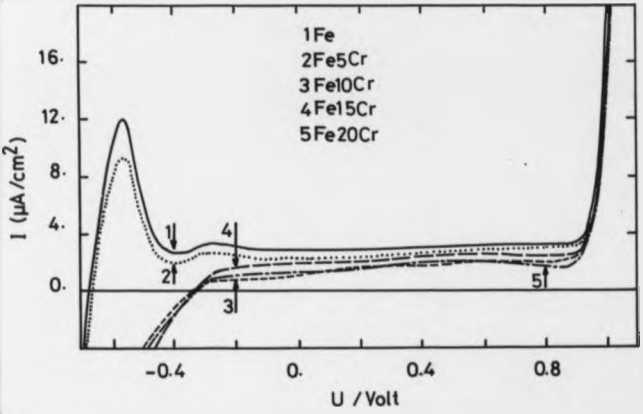

Fig. 4. 7. Polarisation curves in borate buffer solution for 100 λ thick films of Fe and various Fe/Cr alloys evaporated onto mylar substrate.

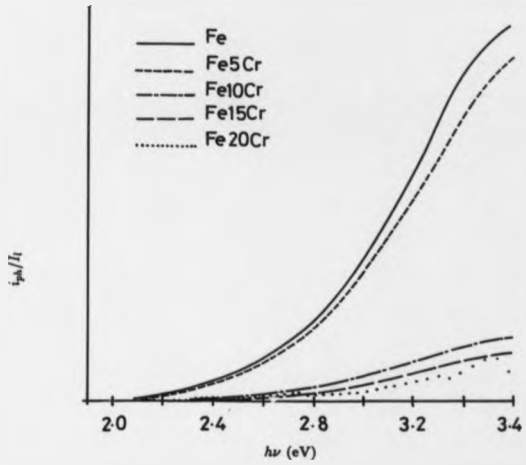

Fig. 4. 8. Energy dependence of the photocurrent spectra, normalised to the lamp emission, for film samples passivated at + 0.9 V in borate buffer solution.

continues to decrease more or less linearly. In this experiment the photocurrent magnitude is relatively small which was probably due to the high reflectivity and low roughness of the samples.

The indirect allowed optical transition between valence and conduction bands was also chosen to process the photocurrent data generated from the film samples. The results of this analysis is illustrated in Fig. 4.9 which presents the $((I_{ph}/I_l).h\nu)^{1/2}$ vs. $h\nu$ plots for pure iron and various iron/chromium alloys. At low energy these plots should be straight lines and when extrapolated to $I_{ph} = 0$ they yield band gap energies listed in Table 4.3. This behaviour is observed for Fe, Fe5%Cr, Fe10%Cr and Fe15%Cr samples and above this composition the data becomes unanalysable. The effective band gap energy for the passive layer is increasing with chromium content but not linearly. In the case of Fe and Fe5%Cr samples band gap energies of 1.92 ± 0.01 and 1.94 ± 0.01 eV were obtained. These values are close to those obtained for iron oxides by other investigations[20,27,69] as well as those obtained in this work for bulk material. However, Fe10%Cr and Fe15%Cr alloys were found to have band gap energies which were 2.09 ± 0.01 and 2.13 ± 0.01 eV respectively. These values do not match up those of iron oxides. The increase of the value of the effective band gap energy for the passive film on high chromium alloys is related to the presence of chromium in the passive film.

4.3.3 The Potential Dependence of the Photocurrent

The potential dependence of the photocurrent was measured for pure iron and iron/chromium alloys prepared as thin films on mylar. These measurements were very difficult to make as the photocurrents were so small. By using the data illustrated in Fig. 4.10 it is not possible to obtain the flat band potential accurately. However, as already stated in section 4.2.3, the values for the flat band potential for this measurement differ by several hundreds of millivolts from those obtained by means of capacity measurements for the bulk material. The I_{ph} vs. U

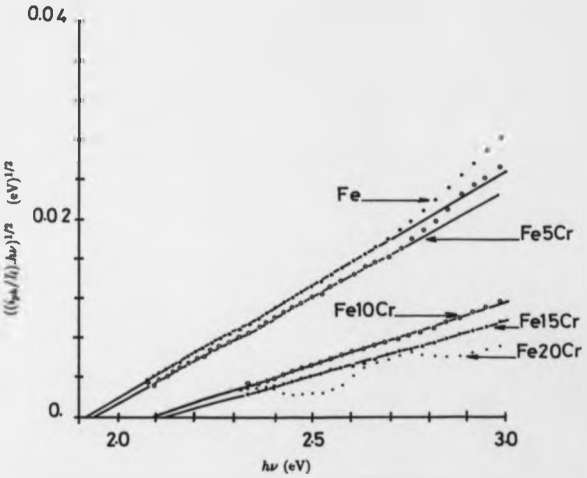

Fig. 4. 9. $((i_{ph}/I_l).h\nu)^{1/2}$ vs. $h\nu$ plots for the film samples passivated at + 0.9 V in borate buffer solution.

E_g^*/eV ($\Delta E_g^* = \pm 0.01$ eV)				
Fe	Fe5%Cr	Fe10%Cr	Fe15%Cr	Fe20%Cr
1.92	1.94	2.09	2.13	

Table 4.3. Apparent optical band gaps of iron and iron/chromium alloy films passivated at + 0.9 V in borate buffer solution.

U_{fb}/volt ($\Delta U_{fb} = \pm 0.05$ V)			
Fe	Fe5%Cr	Fe10%Cr	Fe15%Cr
0.55	0.55	0.30	0.30

Table 4.4. Flat band potentials of iron and iron/chromium alloy films passivated at + 0.9 V in borate buffer solution.

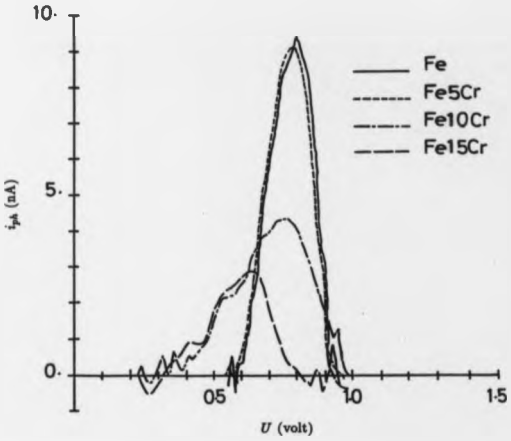

Fig. 4. 10. Potential dependence of the photocurrent spectra for 100 λ thick films of Fe and various Fe/Cr alloys passivated at + 0.9 V in borate buffer. These films were also deposited directly onto mylar substrate.

plots for Fe and Fe5%Cr presented in Fig. 4. 10 are very similar. They both exhibit a peak at 0.75 V and they yield a flat band potential of 0.55 ± 0.05 V (Table 4. 4). These two samples therefore consisted basically of iron oxide type material. In the case of Fe10%Cr alloy the photocurrent magnitude is reduced by 50% which can be explained by either the reduction of the amount of iron present in the passive film or the passive layer on this material is thinner than that formed on pure Fe and Fe5%Cr samples. The I_{ph} vs. U plot for Fe10%Cr shows a peak at 0.75 V which is the same as those for Fe and Fe5%Cr samples but it is broader and has a shoulder located at 0.55 V which can be attributed to chromium oxide. The value of the flat band potential for this sample is 0.30 ± 0.05 V. Further reduction of the photocurrent magnitude was observed in the case of Fe5%Cr and the I_{ph} vs. U plot exhibits a peak at 0.65 V and a shoulder at 0.55 V. The potential dependence of the photocurrent data for this sample yields a flat band potential of 0.30 ± 0.05 V which is similar to that of the passive layer on Fe10%Cr alloy. This suggests that the passive film on high chromium alloy is very rich in chromium.

4.4 Summary

By comparing the electrochemical and photocurrent spectroscopy results, one cannot detect any significant difference between the material prepared as thin films and the bulk one. Furthermore, these results show that the passive film on pure iron is simply a single phase of iron oxide and the one formed on iron/chromium alloys is a mixture of two simultaneous phases of iron and chromium containing oxides. In the case of the alloys, the passive films formed at low potentials were found to be rich in chromium and those formed at high anodic potentials were mainly iron oxides. Perhaps most importantly as far as the present studies are concerned these results indicate that the thin film alloy samples behave essentially identically to the bulk samples. This suggests that conclusions drawn from the structural studies of

passivated film samples discussed in the next chapter should be equally valid for bulk samples.

Chapter 5

X-ray Absorption Spectroscopy Results and Discussion

5.1 Introduction

This chapter is divided in several sections. The second and third are concerned with the use of the model compounds to derive phase shifts and the error analysis respectively. The fourth section presents the *in-situ* and *ex-situ* EXAFS results above the Fe and Cr K-absorption edges for samples passivated by simple immersion whilst the fifth section is devoted to the electrochemical passivation as well as to the *ex-situ* results of the electrodeposited thick FeOOH films. Finally a discussion of the structure of the passive film is given in section six.

5.2 Model Compounds

5.2.1 Iron Oxide Model Compounds

In order to analyse the EXAFS data by using the EXCURVE program[56] phase shifts of the absorbing and backscattering atoms were required. For this purpose a good model compound with a well defined structure from X-ray crystallography is needed. One such compound in the present case is $\alpha-Fe_2O_3$. As already explained in section 2.3.4, phase shifts were calculated

for the absorbing Fe and backscattering O and Fe atoms by using the MUFFPOT program[57]. Subsequently a theoretical EXAFS curve was calculated by using the X-ray crystallographic data derived from the $\alpha-Fe_2O_3$ model compound listed in Table 5.1 and then E_0 was refined to fit the experimental data. When a reasonably good fit was obtained E_0 was fixed and by refining the phase parameters a good fit was obtained which is shown in Fig. 5.1. These new phase shifts were then used in later analyses of the EXAFS data derived from the unknown compounds. The phase shifts calculated by using the MUFFPOT program[57] are usually satisfactory for the analysis. Only minor changes were needed to optimise the fit.

The refined phase shifts were used to fit the EXAFS data derived from $\alpha-FeOOH$ whose structure was also well known from X-ray crystallography. A good fit was obtained by using the parameters listed in Table 5.2. These parameters are very similar to those obtained by X-ray crystallography studies[71]. The same procedure has also been performed on the data derived from $\gamma-FeOOH$ and a good fit was also obtained with similar parameters as those obtained by X-ray crystallography. This has demonstrated the transferability of the phase shifts.

The phase shifts obtained for the $\alpha-Fe_2O_3$ model compound were then used later in the data analysis. Since all spectra in this work were calibrated to that of the $\alpha-Fe_2O_3$ model compound the energy correction, ΔE_0, derived for this compound was kept constant for all analyses. Since the edge positions for all samples and model compounds were identical this corresponds to assuming the same E_0 for the photoelectron.

5.2.2 Chromium Oxide Model Compound

$\alpha-Cr_2O_3$ was the model compound chosen to derive phase shifts for the analysis of the EXAFS data measured above Cr K-absorption edge. The same procedure as in section 5.2.1 above was followed and phase shifts for the absorbing Cr and backscattering Cr and

s = shell no.	Type of atom	N_s	R_s (λ)	A_s (λ^2)
1	O	3	1.95	0.014
2	O	3	2.11	0.020
3	Fe	1	2.90	0.026
4	Fe	3	2.97	0.016
5	Fe	3	3.96	0.010
6	O	3	3.40	0.004
7	O	3	3.59	0.008
8	Fe	6	3.70	0.026

Table 8. 1. Structure parameters around an Fe atom in $\alpha-Fe_2O_3$ [71].

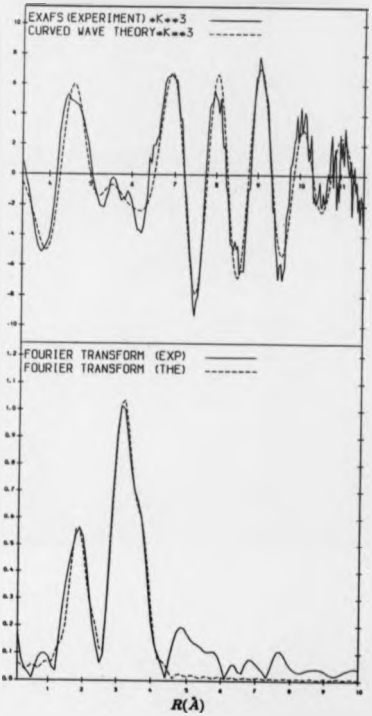

Fig. 5. 1. k^3 weighted EXAFS spectrum above Fe K-absorption edge for $\alpha-Fe_2O_3$ model compound and the best fit theoretical curve. The corresponding Fourier transforms are also shown.

s = shell no.	Type of atom	N_s	R_s (Å)	A_s (Å^2)
1	O	2	1.96	0.008
2	O	4	2.09	0.019
3	Fe	4	3.05	0.022
4	Fe	4	3.39	0.025
5	O	6	3.78	0.024

Table 5. 2. Structure parameters around an Fe atom in α−FeOOH [71].

s = shell no.	Type of atom	N_s	R_s (Å)	A_s (Å^2)
1	O	6	1.99	0.009
2	Cr	4	2.83	0.015
3	Cr	9	3.59	0.021
4	O	9	3.80	0.021

Table 5. 3. Structure parameters around a Cr atom in α−Cr_2O_3 [72].

O atoms were obtained when the fit shown in Fig. 5.2 was achieved with the parameters listed in Table 5.3, the bond distances being those obtained from X-ray diffraction studies[72]. Basically the phase shifts were calculated by using only the first two shells as the same results were achieved when more shells were introduced. Here again the phase shifts calculated by using MUFFPOT program[57] only required minor refinements to optimise the fit. However, model compounds are always needed for direct comparison of the EXAFS and XANES data with those of the unknown. For this reason more model compounds were used in this work. These compounds were $Cr(OH)_3$, K_2CrO_4 and $K_2Cr_2O_7$.

The use of the $\alpha-Cr_2O_3$ model compound was also beneficial in the EXAFS data calibration and the energy correction ΔE_0 obtained for this compound was used, as in the case of the Fe K-absorption edge data, to correct the EXAFS data above the Cr K-absorption edge derived from the unknown compounds in later analyses.

5.3 Error Analyses

Before discussing the results it is very important to consider the errors. Usually the absolute error on bond distances obtained by Fourier transforming EXAFS data is of the order of $\Delta R = \pm\ 0.02\ \AA$ for first and second shells. However, in the present work where trends in bond lengths are important this overestimates relative errors. The calculation of bond lengths depends on many variables. One such variable is the energy correction factor ΔE_0. In the present work the uncertainty of the bond distances as a function of E_0 is comparable with $\Delta R \simeq \pm\ 0.02\ \AA$. For this reason it is very important to calibrate the EXAFS spectra to that of the model compound and to fix the energy correction factor ΔE_0 to that obtained for the model compound. Having E_0 constant, the error on the variation of the bond distances becomes smaller. By comparing the experimental data to the theoretical calculations the bond distances were obtained with an average $\Delta R \simeq \pm 0.005 \AA$. However, bearing in mind

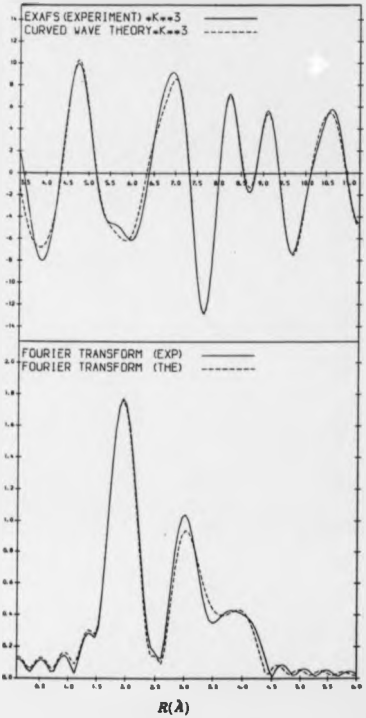

Fig. 5.2. k^3 weighted EXAFS spectrum above Cr K-absorption edge for $\alpha-Cr_2O_3$ model compound and the best fit theoretical curve.

the uncertainty on E_0 obtained from the model compound the variation in bond distances is going to be larger but not more than $\Delta R \simeq \pm 0.01 \AA$. Within this uncertainty the variation of the bond distances as a function of the composition of the samples can be discussed.

5.4 The In-situ and Ex-situ EXAFS Results of the Passive Film Formed on Pure Fe and Fe/Cr Alloys by Simple Immersion in Solution

5.4.1 Introduction

The solutions used for the passivation by simple immersion were sodium nitrite and potassium chromate. The films formed in these solutions are thought to have similar structure to those formed anodically in solutions free from Fe^{2+} ions[84]. It is therefore convenient to present the results of these films prior to those obtained in the rather more complex electrochemical experiments. Since EXAFS spectra were recorded above both Fe and Cr K-absorption edges, the results as well as their discussion are presented in two subsections.

5.4.2 Results and Discussion of Fe and Fe/Cr Alloy Films at Fe K-Absorption Edge

5.4.2.1 Wet Films Formed in 0.1M $NaNO_2$

The EXAFS data measured above Fe K-absorption edge for the passive film on pure Fe and various Fe/Cr alloys gave easily the first Fe-O and Fe-Fe bond distances which are shown in Table 5.4. From this table it can be seen that the first Fe-O and Fe-Fe bond lengths for pure Fe are found to be 1.99 $\AA \pm$ 0.01 $\AA$ and 3.03 $\pm$ 0.01 $\AA$ respectively. This first Fe-O bond distance is very similar to those obtained for $\alpha - Fe_2O_3$ and $\gamma - FeOOH$ model compounds but the first Fe-Fe bond length was higher than that of $\alpha - Fe_2O_3$ (2.92 $\pm$ 0.01 $\AA$) and lower than

	Fe-O			Fe-Fe		
	N_1	R_1 (Å)	A_1 (Å^2)	N_2	R_2 (Å)	A_2 (Å^2)
Fe	6	1.98	0.019	6	3.03	0.057
Fe5%Cr	6	2.01	0.022	6	3.02	0.039
Fe10%Cr	6	2.00	0.019	6	3.05	0.039
Fe15%Cr	6	2.01	0.026	6	3.05	0.050
Fe25%Cr	6	2.02	0.028	6	3.07	0.058
γ−FeOOH	6	2.04	0.018	6	3.09	0.014

Table 5. 4. Structure parameters obtained from *in-situ* measurements for Fe and Fe/Cr alloys passivated in 0.1 M $NaNO_2$ by *simple* immersion. The parameters for γ−FeOOH are also shown.

	Fe-O			Fe-Fe		
	N_1	R_1 (Å)	A_1 (Å^2)	N_2	R_2 (Å)	A_2 (Å^2)
Fe	6	2.02	0.021	6	3.03	0.039
Fe15%Cr	6	2.00	0.021	6	3.06	0.061
Fe25%Cr	6	2.00	0.020	6	3.08	0.051

Table 5. 5. Structure parameters obtained from *ex-situ* measurements for samples passivated in 0.1 M $NaNO_2$ solution.

that of γ−FeOOH (3.09 ± 0.01 Å) model compound. From these values it can be deduced that the passive film on Fe formed by simple immersion in nitrite solution is not a simple stoichiometric Fe(III) oxide or hydroxide.

The Fe5%Cr alloy shows similar results to pure Fe but as the Cr content increases the first Fe-Fe distance increases whilst the first Fe-O distance remains constant. This distance is found to be 3.05 ± 0.01 Å for both Fe10%Cr and Fe15%Cr alloys and 3.07 ± 0.01 Å for Fe25%Cr. For all compositions the first shell was easily fitted with six oxygen atoms and the second with six Fe atoms. Slightly better fits can be achieved by changing the number of Fe atoms in the second shell without changing the number of oxygen atoms in the first shell. At no time was any evidence obtained for more than two shells contributing to EXAFS. This is clearly shown in Fig. 5.3 for the Fe5%Cr passivated alloy where a good fit to EXAFS data was obtained for low k range. Above $k = 7\text{Å}^{-1}$ the oscillations are very weak and rather less well fitted. The weakness of the oscillations in this region arises from the decay of the EXAFS and cancellation effects between the two shells which are largely out of phase with each other in this region. The EXAFS for all samples exhibit this feature though the exact form of the oscillations in this region vary for samples corresponding to different alloy compositions as the degree of cancellation is very sensitive to the relative values of the Debye-Waller factor. This effect will be discussed further in section 5.5.3. This suggests that there is only a short range order in the structure of the passive films. However, the first shell parameters show clearly that the basic [FeO_6] octahedra units are conserved and these are probably linked together in a disordered manner to form a three dimensional structure.

5.4.2.2 Dry Films Formed in 0.1M $NaNO_2$

The Fe, Fe5%Cr and Fe25%Cr passivated samples were chosen for an *ex-situ* fluorescence EXAFS investigation. The results of these investigations listed in Table 5.5 are very similar

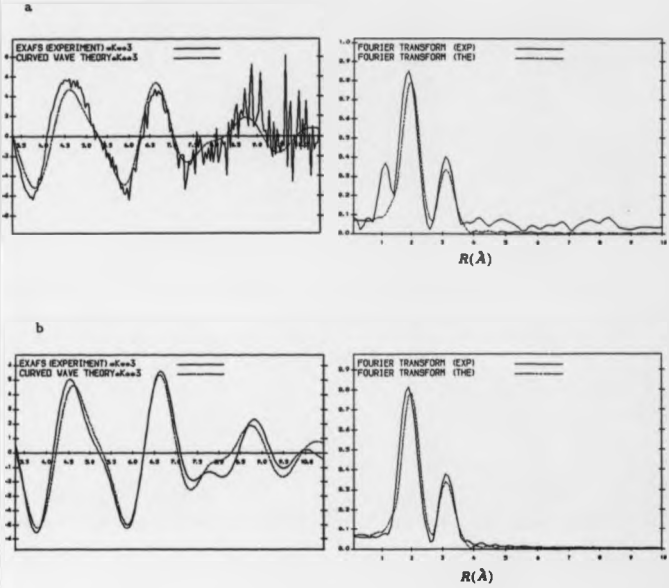

Fig. 6.3. k^3 weighted EXAFS spectrum above Fe K-edge for Fe5%Cr passivated by immersion in 0.1 M $NaNO_2$. (a) and (b) show the raw and filtered data respectively with the best fit theoretical curves as well as the corresponding Fourier transforms.

to those obtained in the case of the wet passive films. For all samples here again the first shell was fitted with six oxygen atoms at a distance of 2.00 ± 0.01 $\AA$ and the second shell was also fitted with six Fe atoms at a distance increasing with the Cr content. This distance was found to be 3.03 ± 0.01 $\AA$, 3.05 ± 0.01 $\AA$ and 3.08 ± 0.01 $\AA$ for Fe, Fe15%Cr and Fe25%Cr alloys respectively. A better fit has also been obtained by altering slightly the number of Fe atoms in the second shell. These results show that the structure of the passive film appears to remain the same even after its removal from the solution and after it has been dried in a good vacuum, i.e. the structure of the dried passive films formed in nitrite is similar to that of the wet ones in the same solution.

5.4.2.3 Wet Films Formed in 0.005M K_2CrO_4

Unlike the nitrite-formed passive films, the chromate-formed ones seem to have the same structure at all compositions. The EXAFS data derived from pure Fe and Fe/Cr alloys were well fitted by using six oxygen atoms at an average Fe-O distance of 1.99 ± 0.01 $\AA$ for the first shell and six Fe atoms at an average Fe-Fe distance of 3.02 ± 0.01 $\AA$ for the second shell. These results are summarized in Table 5.6 and they lend support to a disordered structure of the passive film. The structural similarities shown for all chromate-formed passive films can be related to the amount of chromium in the passive film which is probably similar in all samples as will be shown later, chromium is incorporated in the film from the chromate solution. Even in the case of pure Fe sample it seems that the concentration of chromium in the passive film is similar to that of high chromium alloys. This can be shown in Fig. 5.4 where the Cr K-absorption edge amplitude looks similar for all samples passivated in the chromate solution. It is interesting to note that the Fe-Fe distance in the chromate passivated samples is similar to that for pure iron passivated in nitrite rather than a high chromium content alloy. This effect of chromium in solution seems to differ from its effect when present in solution.

	Fe-O			Fe-Fe		
	N_1	R_1 (Å)	A_1 (Å^2)	N_2	R_2 (Å)	A_2 (Å^2)
Fe	6	2.00	0.022	6	3.02	0.048
Fe5%Cr	6	1.99	0.018	6	3.02	0.046
Fe10%Cr	6	1.99	0.021	6	3.02	0.051
Fe15%Cr	6	2.00	0.027	6	3.04	0.045
Fe25%Cr	6	2.00	0.025	6	3.03	0.058

Table 5.6. Structure parameters obtained from *in-situ* measurements for samples passivated in 0.005 M K_2CrO_4.

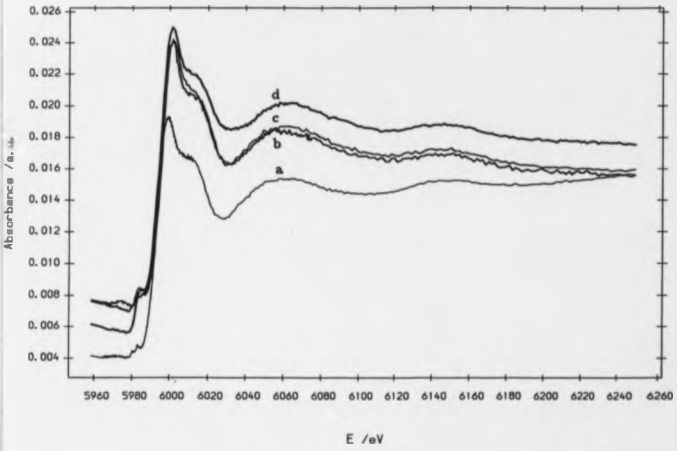

Fig. 5. 4. Ex-situ X-ray absorption spectra at Cr K-edge, using the fluorescence mode, for (a) Fe, (b) Fe15%Cr and (c) Fe25%Cr dipped in 0.005 M K_2CrO_4.

5.4.3 Ex-situ and In-situ EXAFS Results at Cr K-Absorption Edge and their Discussion

For all samples passivated in potassium chromate solution it was necessary to wash and dry the samples prior to the analysis otherwise chromate ions in solution would contribute to the X-ray absorption. For high Cr content alloys passivated in nitrite solution it was possible to record spectra *in-situ*.

5.4.3.1. Samples Passivated in 0.005M K_2CrO_4

a. Bulk and Film of Pure Fe

A significantly large K-absorption edge of Cr was measured from a bulk iron sample immersed in chromate solution for one week. The X-ray absorption spectrum at the Cr K-edge using fluorescence detection is shown in Fig. 5.4. The large Cr K-edge as well as the strong EXAFS oscillations obtained for this sample indicate clearly that Cr has been incorporated in the passive film from the potassium chromate solution.

By analysing the EXAFS data (Fig. 5.5) a good fit was obtained by calculating a theoretical EXAFS spectrum in k-space by using two atomic shells. The first was an oxygen shell containing six atoms at Cr-O distance of 1.99 ± 0.01 $\AA$ and the second was split into two Cr shells containing three atoms each at Cr-Cr distances of 2.91 ± 0.01 $\AA$ and 3.10 ± 0.01 $\AA$ respectively. The first Cr-O distance is similar to those obtained for any chromium oxide or hydroxide (Table 5.7) and the coordination number six indicates that the basic $[CrO_6]$ octahedra units are also conserved here just as it has been shown earlier by the EXAFS data measured above Fe K-edge. The second shell can be fitted with Cr atoms only if it is split into two shells and the distances obtained for these shells match up very well those of the amorphous $Cr(OH)_3$ but not those of $\alpha-Cr_2O_3$ model compound whose data are shown in Fig. 5.6. It can be concluded that the octahedra units $[CrO_6]$ in the film are linked together

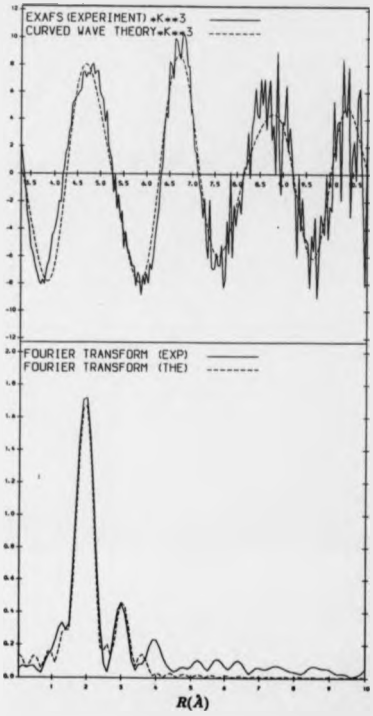

Fig. 5.5. EXAFS spectrum above Cr K-edge and its Fourier transform for an Fe foil dipped in 0.005 M K_2CrO_4 solution. The dashed lines represent the fit theoretical curves.

	Cr-O			Cr-Cr			Cr-Cr		
	N_1	R_1 (Å)	A_1 (Å^2)	N_2	R_2 (Å)	A_2 (Å^2)	N_3	R_3 (Å)	A_3 (Å^2)
$Cr(OH)_3$	6	1.99	0.011	3	2.92	0.014	3	3.10	0.026
Fe(foil)	6	1.99	0.009	3	2.91	0.015	3	3.10	0.022
Fe	6	1.99	0.007	3	2.90	0.015	3	3.08	0.024
Fe15%Cr	6	1.99	0.013	3	2.90	0.016	3	3.08	0.025
Fe25%Cr	6	1.99	0.017	3	2.91	0.015	3	3.09	0.025

Table 5.7. Structure parameters obtained for $Cr(OH)_3$ compound, Fe foil and film samples passivated in 0.005 M K_2CrO_4 by simple immersion. The measurements were made *ex-situ*.

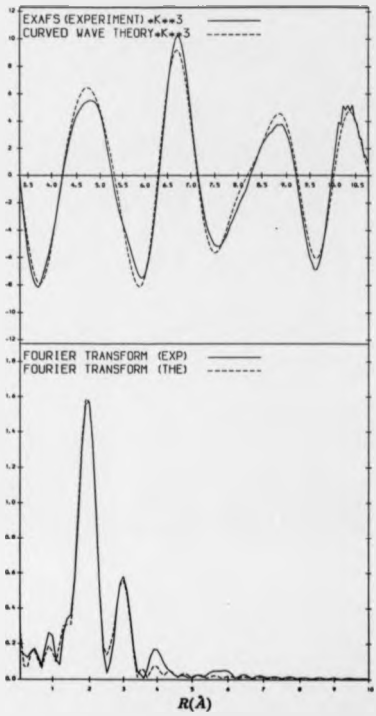

Fig. 5.6. EXAFS spectrum above Cr K-edge and Fourier transform for commercial $Cr(OH)_3$ compound. The best fit theoretical curves are also shown.

by hydrogen bonds just as for the amorphous hydrous oxide $Cr(OH)_3$.

Similar results were obtained for an Fe sample prepared as a thin film. The EXAFS data derived from this sample were also fitted with three shells. The first one has six oxygen atoms at Cr-O distance of 1.99 ± 0.01 Å and the second and third shells were fitted with three Cr atoms each at Cr-Cr distance of 2.90 ± 0.01 Å and 3.08 ± 0.01 Å respectively. These results are also summarised in Table 5.7.

b. Fe15%Cr and Fe25%Cr Alloys

The EXAFS results derived from Fe15%Cr and Fe25%Cr alloys at Cr K-absorption edge are shown in Table 5.7 together with those of the bulk and thin film iron samples immersed in chromate solution. The bond lengths as well as Debye-Waller factors obtained for these alloys are within experimental error very similar to those of pure iron passivated in the same solution. Therefore the structure of the chromium containing part of the passive film formed in chromate solution is the same at all compositions. It has a disordered structure similar to that of the commercially available $Cr(OH)_3$ compound.

One of the most interesting features observed for all samples passivated in K_2CrO_4 solution is the similarity in the Cr K-edge height regardless of the composition. This is illustrated in Fig. 5.4 and indicates that the quantity of Cr present in the passive film on pure iron is similar to that present in the passive film formed on high Cr content alloys. Therefore the Cr that enhances the passivity is either provided by the alloy itself or incorporated in the sample from chromate solution.

5.4.3.2. Fe25%Cr Alloy Passivated in 0.1M $NaNO_2$

Since Cr present in the passive film formed in nitrite solution comes only from the alloy itself, Fe25%Cr alloy was chosen to study the influence of Cr on the structure of the passive film that forms on Fe/Cr alloys immersed in nitrite solution.

The *ex-situ* EXAFS measured above the Cr K-edge are shown in Fig. 5.7. It was very difficult to obtain a good fit but similar bond lengths as well as the coordination numbers to those for the passivated samples in chromate solution were obtained (Table 5.8). However, the Debye-Waller factor in this case is found to be higher for the first oxygen shell and those for the second and third Cr shells were found to be smaller. By using a single shell analysis, it was easy to fit the first oxygen shell with six atoms at a distance of 1.98 ± 0.01 $\AA$ which is the same as that found for all samples passivated in chromate solution but the Debye-Waller factor for this shell was higher. As more shells were introduced in the analysis the fit became difficult. Although the main structure can be fitted with similar parameters to those obtained for the potassium chromate passivated samples it appears that a Cr shell was needed at Cr-Cr distance of 2.50 $\AA$. This shell corresponds to the first nearest neighbour distance found in Cr metal. This suggests that there is some Cr still present in the passive film as metallic phase. However, it is not possible to introduce such a shell in the analysis as the choice of E_0 becomes a problem since it varies as the oxidation state of the material varies. Hence it is not easy to draw conclusions about the structure of the passive film formed on this sample but it is interesting that the nitrite solution aids the passivation and not more than 25%Cr is needed in an Fe/Cr alloy to obtain a good passivation in nitrite solution.

More difficulties were found in the analysis of the EXAFS data, for this sample, measured *in-situ*. Similar parameters to those of the dry sample were obtained for the first shell but slightly shorter bond lengths as well as lower Debye-Waller factors for the second and third shells. The poor fit may also be attributed to the existing metallic Cr phase in the film and the slight difference in the structure may be associated with the water contained within the film.

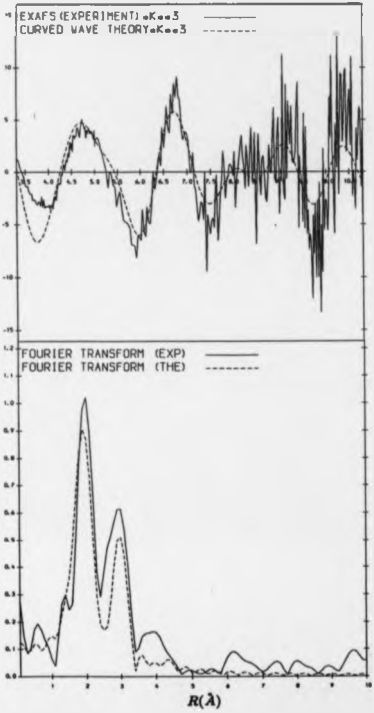

Fig. 5. 7. Experimental and theoretical EXAFS spectra above Cr K-edge and the corresponding Fourier transforms for an Fe25%Cr alloy passivated in 0.1 M $NaNO_2$ solution.

	Cr-O			Cr-Cr			Cr-Cr		
	N_1	R_1 (Å)	A_1 (Å^2)	N_2	R_2 (Å)	A_2 (Å^2)	N_3	R_3 (Å)	A_3 (Å^2)
Fe25%Cr(dry)	6	1.98	0.023	3	2.87	0.007	3	3.06	0.014
Fe25%Cr(wet)	6	1.98	0.023	3	2.84	0.004	3	3.01	0.005

Table 6. 8. Structure parameters obtained both *in-situ* and *ex-situ* for the Cr phase in Fe25%Cr alloys passivated in 0.1 M $NaNO_2$.

5.5 The Electrochemical Passivation Results and Discussion

5.5.1 Electrochemical Behaviour

The polarisation curves of the thin films deposited on a Au film on mylar were recorded in order to check their electrochemical behaviour. These films were found to behave in a similar way to the films deposited directly onto clean mylar. Fig. 5.8 shows polarisation curves in the borate buffer for Fe film on mylar, Au film on mylar and Fe film on Au onto mylar. This figure shows clearly that in the passivation of the film deposited on Au on mylar, Au was exposed but all iron features were retained. In fact the polarisation curve for Fe on a gold film can be obtained by superimposing the two curves obtained for Fe and Au films separately. The exposure of gold is believed to be due to the uneven distribution of the iron film as well as the edges of the sample, especially as the thickness of the Fe film is only 20 Å. Similar results to these were obtained for the electrochemical passivation in the sodium perchlorate solution and Fig. 5.9 shows the results for an iron film deposited on gold on a mylar flag passivated in this solution. Here again all iron features were observed.

5.5.2 Fe and Fe25%Cr Samples Passivated in Borate Buffer Solution (pH 8.4)

Pure Fe and an alloy containing 25% Cr were passivated in a borate buffer solution (pH 8.4), the EXAFS data were analysed and the results obtained are shown in Table 5.9. It has been suggested[6] that since cathodic polarisation of Fe, to remove the air formed oxide prior to anodising, releases Fe^{2+} ions into the solution this leads to a different passive film to that formed in Fe^{2+} free solutions, in particular it has been claimed that this leads to the formation of the oxyhydroxide rather than the oxide. To test this hypothesis some cells were drained of electrolyte after cathodising, whilst maintaining the potential as much as possible and flushing with argon to prevent the entry of air, before being refilled with new solution prior

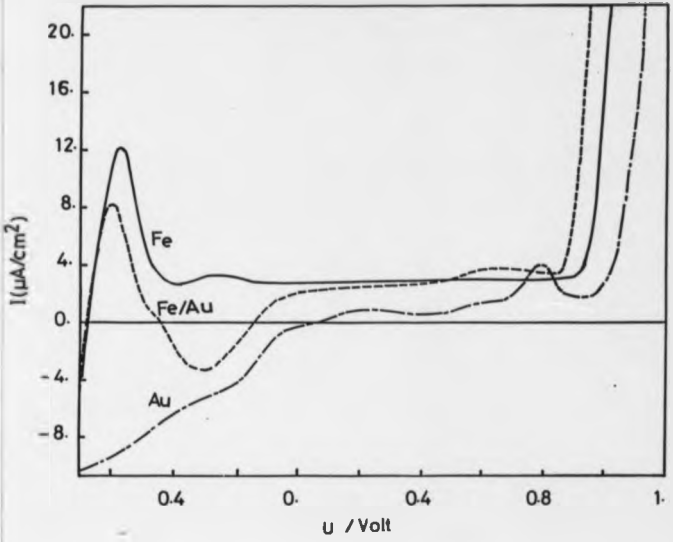

Fig. 5. 8. Polarisation curves in borate buffer solution for a 100 Å thick film of Fe on mylar, a 200 Å thick film of Au on mylar and a 20 Å thick film on gold on mylar.

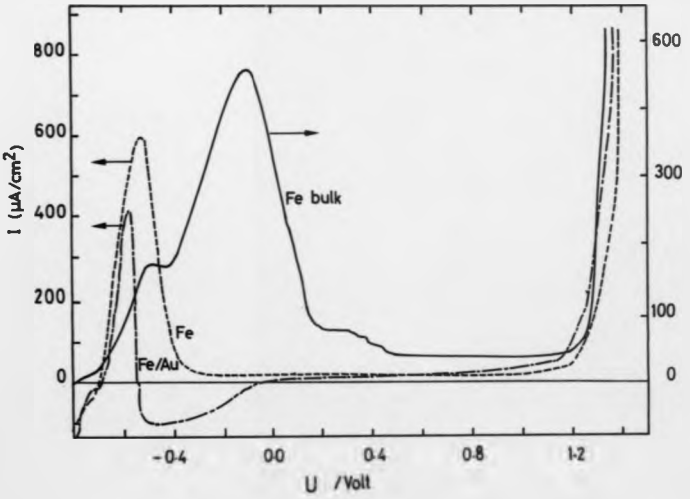

Fig. 5. 9. Polarisation curves in sodium perchlorate for bulk iron, 100 Å thick film of iron and 20 Å thick film of iron evaporated on gold.

	Fe-O			Fe-Fe		
	N_1	R_1 (Å)	A_1 (Å^2)	N_2	R_2 (Å)	A_2 (Å^2)
Fe passivated in borate solution	6	2.02	0.020	6	3.05	0.030
Fe25%Cr passivated in borate solution	6	2.02	0.020	6	3.05	0.044
Fe passivated in perchlorate solution	6	2.01	0.024	6	3.02	0.036
Fe25%Cr passivated in perchlorate solution	6	2.02	0.021	6	3.05	0.046
FeOOH deposited from borate + Fe^{2+}	6	2.02	0.024	6	3.04	0.043
FeOOH deposited from $(NH_4)_2SO_4$ + Fe^{2+}	6	2.00	0.014	6	3.02	0.046

Table 5.9. Structure parameters obtained *in-situ* for Fe and Fe25%Cr samples passivated electrochemically at + 0.9 V in both the borate buffer and 0.1 M $NaClO_4$ solution. Those obtained *ex-situ* for FeOOH samples electrochemically deposited from borate and $(NH_4)_2SO_4$ solutions containing Fe^{2+} ions are also shown.

to anodising the sample. The results obtained in this way were identical to those obtained without this precaution.

Fig. 5.10 shows absorption spectra in the region of the Fe K-absorption edge of an iron film, cathodically protected at −0.7 V in borate buffer solution, and then passivated by stepping the potential to 0.8 V. The expected shift of the position of the absorption edge to higher energies on oxidation is clearly seen. From Table 5.9 it can be seen that the structure of the passive film seems to be independent of the chromium content, the second shell radius being long even for the pure Fe film. This lack of sensitivity to the Cr content is possibly due to the incorporation of boron (B) into the film. Films on pure Fe have also been studied as a function of the electrode potential and there appears to be no variation in the structure with potential, though of course there is a change in film thickness.

5.5.3 Fe and Fe25%Cr Samples Passivated in Sodium Perchlorate Solution

As for all Fe K-edge EXAFS data discussed in this chapter the data presented in this section is also fitted with only two shells. Fig. 5.11 shows the EXAFS data in k-space as well as the Fourier transform for pure Fe sample anodically passivated in sodium perchlorate solution. Here again the data show only two well defined oscillations, as the contributions from the two shells effectively cancel each other at k greater than 7 $\AA^{-1}$. This can be demonstrated by Fig. 5.12 where the two shells were plotted individually as well as their sum. The results obtained for both pure iron and Fe25%Cr passivated in perchlorate solution are also shown in Table 5.9. These samples seem to behave in a similar way to those passivated by simple immersion in sodium nitrite solution, that is the second shell radius increases with increasing Cr content.

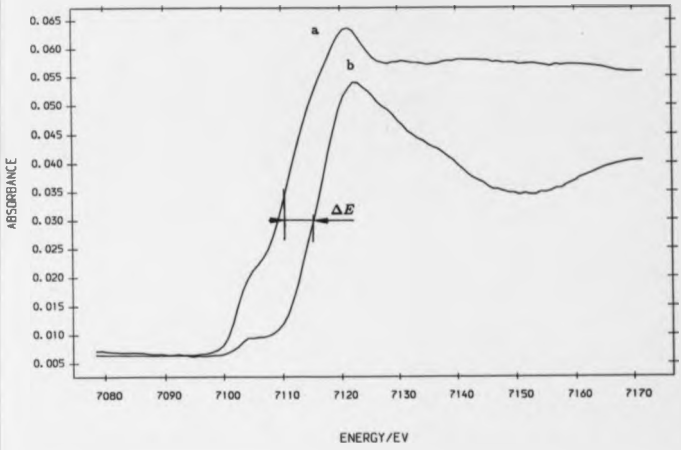

Fig. 5. 10. X-ray absorption spectra in the region of the Fe K-edge for (a) a 20 Å Fe film at −0.7 V in borate buffer and (b) the same film at + 0.8 V.

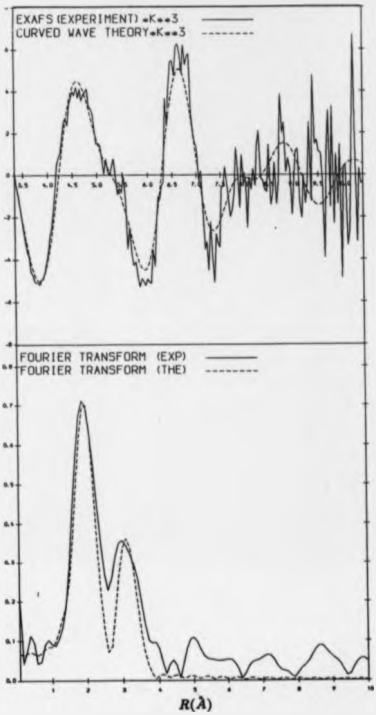

Fig. 5.11. k^3 weighted EXAFS spectra for Fe film at + 0.8 V in sodium perchlorate and the corresponding Fourier transforms.

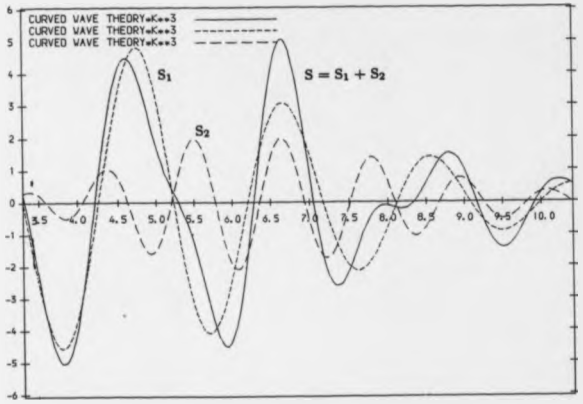

Fig. 5.12. k^3 weighted theoretical EXAFS spectra for Fe film at + 0.8 V in perchlorate. S_1 and S_2 represent the theoretical first and second shells contribution respectively.

5.5.4 γ–FeOOH Films Electrodeposited from Fe^{2+} Containing Borate Buffer and Ammonium Sulphate Solutions

These films were studied for comparison purposes. Their thicknesses were approximately 500 $\AA$. The film formed in borate buffer has already been shown to contain boron[66] whilst that formed from sulphate solution is thought to be free from incorporated species[67]. The fluorescence EXAFS of these samples were recorded *ex-situ* and the results of the analysis are also given in Table 5.9. By referring to this table it can be seen that the oxygen first shell is similar to those of all samples studied in this work. However, the second shell radius is greater for the sample formed in borate whilst the value for that grown from sulphate is comparable with that for the passive film formed on pure Fe by simple immersion in nitrite, or electrochemically in perchlorate.

5.6 Discussion of the Structure of the Passive Film on Fe and FeCr Alloys

5.6.1 Fe K-Absorption Edge

5.6.1.1 Film Formed on Iron

The chemical shift of +5 eV obtained by comparing the near edge structure (XANES) spectra in Fig. 5.10 of the passivated and cathodically protected Fe sample in borate buffer is caused by the oxidation of Fe to Fe^{3+}. Fig. 5.13 shows the comparison of the XANES spectrum of an electrochemically passivated Fe film in sodium perchlorate solution with spectra for various model compounds. This indicates that the spectrum for the passive film is more like that for the oxyhydroxides than oxides, and from detailed examination it appears to be most like that for γ–FeOOH. Similar observations were made for all pure Fe samples passivated in various solutions. These results therefore lend support to the idea that the passive film on Fe has a

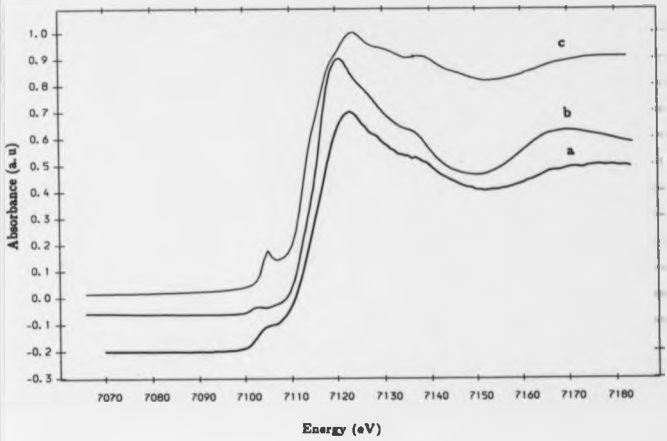

Fig. 5. 12. XANES spectra at Fe K-edge for, (a) a 20 Å Fe film at + 0.8 V in perchlorate solution, (b) γ−FeOOH and (c) γ−Fe_2O_3.

structure like that of an oxyhydroxide. The EXAFS analysis however can give more detailed information about the structure.

To fit the EXAFS data for all passivated iron samples, two shells were required. The first one was an oxygen shell containing six atoms at an Fe-O distance of 2.00 $\AA$ and the second Fe shell with six atoms at an Fe-Fe distance of 3.02 $\AA$. By considering only these bond lengths it is not easy to identify the structure of the passive film as in most iron oxides and hydroxides the structure is based on basic octahedra units of oxygen atoms surrounding the iron centre and therefore the radii for the first shells are very similar. The second shells have radii that range from 2.95 $\AA$ for $\alpha-Fe_2O_3$ to 3.09 $\AA$ for $\gamma-FeOOH$ but a large variation occurs in the third shell. This results from the way $[FeO_6]$ octahedra units are linked together to form an extended three dimensional structure of different compounds. These differences are better shown by comparing the atomic radial distribution functions (RDF's) which are calculated from the best fit to the EXAFS data. Fig. 5. 14 indicates clearly that apart from the passive film and $\gamma-FeOOH$ RDF's for all other structures exhibit an atomic shell in the region of 3.4 $\AA$ due to the large contribution of Fe atoms. It is important of course to bear in mind that in $\gamma-FeOOH$ structure a number of oxygen atoms are present in this region but their contribution to the EXAFS is not significant. The calculated RDF peaks for $\gamma-FeOOH$ and the passive film are in very similar positions. However, those for the passive film are shorter and broader especially that for the second shell. This indicates that the passive film has a disordered structure. On the basis of these EXAFS data it can be concluded that the passive film formed on Fe, either by immersion or electrochemically, has a structure like disordered $\gamma-FeOOH$. That is $[FeO_6]$ octahedra linked, by sharing edges, into sheets or chains but probably not into an extended three dimensional structure.

The conclusion drawn in the present work is in disagreement with that reached in the work of Long *et al*[9] and Kruger *et al*[11] where it has been claimed that the passive film

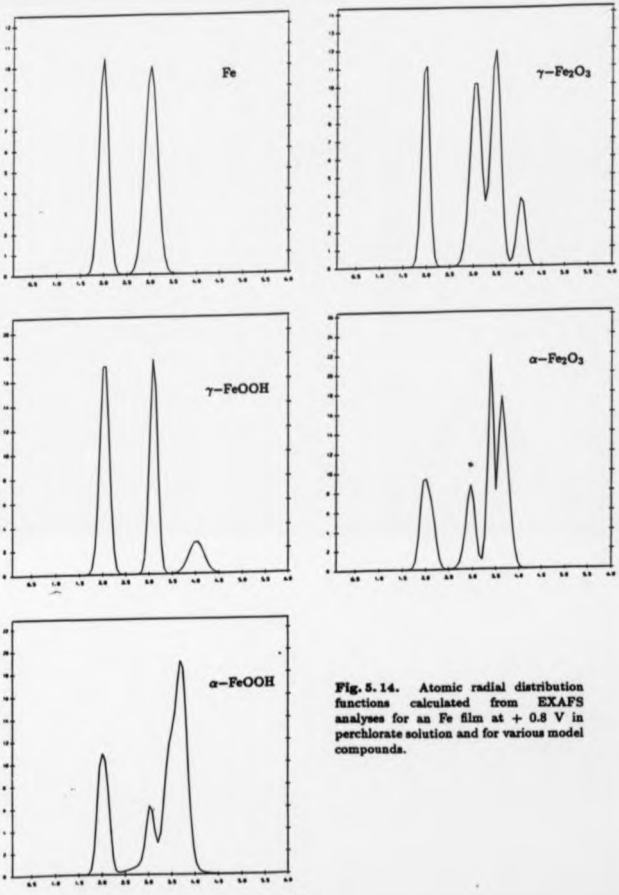

Fig. 5. 14. Atomic radial distribution functions calculated from EXAFS analyses for an Fe film at + 0.8 V in perchlorate solution and for various model compounds.

undergoes structural changes from disordered γ−FeOOH to disordered γ−Fe_2O_3 as the film was removed from the solution for the *ex-situ* X-ray absorption measurements. However, in their investigations the samples were not converted completely into passive film since they formed an extra peak in the Fourier transform which corresponds to the first Fe-Fe distance in metallic iron. The presence of the mixed phase structure in their samples makes the analysis difficult. Moreover, the use of the glass substrate, in their work, introduces even more difficulties as in this work it is found that it contains enough iron to give a signal comparable in magnitude to that from the passive film.

5.6.1.2 Film Formed on Fe/Cr Alloys

As expected the chemical shift as well as the XANES for Fe/Cr alloys are found to be similar to that for pure Fe samples. The EXAFS data in all cases were fitted with six oxygen atoms in the first shell and six iron atoms in the second. The only significant changes with composition are found for samples passivated in sodium nitrite solution where the second shell, initially much shorter than that for γ−FeOOH, increases in radius with increasing chromium content. However, no similar trend is seen for the passivation in potassium chromate solution. The interesting point to note is that the *ex-situ* results of the nitrite passivated samples were essentially identical to those of the *in-situ* ones indicating that drying does not affect significantly the structure of these films, at least as determined by the EXAFS analysis. Here again the EXAFS data as well as the XANES show that the passive film formed on Fe/Cr alloys, either by simple immersion or electrochemically, has a structure like disordered γ−FeOOH just as that formed on pure Fe.

5.6.2 Cr K-Absorption Edge

The XANES spectra at the Cr K-edge for an Fe foil that had been immersed in potassium chromate solution and some model compounds are shown in Fig. 5.16. From the edge energy

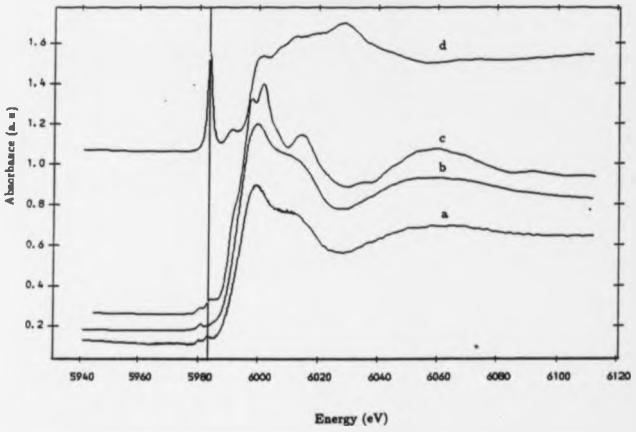

Fig. 5.15. XANES spectra at Cr K-edge for (a) an Fe foil dipped in K_2CrO_4 solution, (b) $Cr(OH)_3$, (c) Cr_2O_3 and (d) K_2CrO_4.

positions it can be seen that Cr in the passive film is present as Cr^{3+}. By examining the XANES it appears that the passive film has similar structure to the amorphous $Cr(OH)_3$ compound, rather than Cr_2O_3. In this figure there are some small pre-edge peaks in the spectra for the passive films and one of these in each spectrum aligns up very well in energy with the sharp peak seen for the tetrahedral environment for Cr^{6+} species. This suggests that there is also a small amount of Cr^{6+} present in this passive film. This particular peak seems to appear only for samples that have been exposed to solutions containing Cr^{6+} and not for samples where the alloy is the source of the Cr. Since this Cr^{6+} in the film has survived a thorough washing procedure it is most probably present as a strongly adsorbed phase. A similar observation has been made for aluminium samples exposed to Cr^{6+} containing solutions[73]. The absence of this peak for samples where the source of Cr is the alloy itself indicates, however, that this adsorbed Cr^{6+} probably plays no significant role in corrosion inhibition.

Further information on the structure of the Cr containing part of the passive film were obtained from the EXAFS analysis. All EXAFS data at Cr K-absorption edge match up very well those for commercial $Cr(OH)_3$ rather than those for Cr_2O_3. From Table 5.7 and 5.8 it can be seen that all parameters used to obtain the best fit were identical, within an experimental error, except for some variation in the Debye-Waller factors for the second shell, implying a possible variation in the disorder. Therefore it can be deduced that the structure of the Cr containing part of the passive film is very similar to that of $Cr(OH)_3$. Hence this structure is based on $[CrO_6]$ octahedra units linked together by hydrogen bonds as it is the case for the known amorphous $Cr(OH)_3$. It is therefore this amorphous phase that seems to be responsible for the improved corrosion resistance of Cr containing Fe alloys. The EXAFS data for high Cr content alloys were not easy to fit as there was Cr present in the passive film as a metallic phase.

Chapter 6

Conclusions and Suggestions for Further Work

The electrochemical behaviour of iron and iron/chromium alloys prepared as thin films has been shown to be similar to that of the bulk material, whilst the photocurrent spectroscopy studies of the two types of material have also led to the same conclusions. These results would appear to justify the extension of the conclusions of the EXAFS study of the thin film materials to the passive film formed on bulk material. The use of this thin film approach to the EXAFS study of the passive film on Fe was first proposed by Long et al[6] but the suitability of this does not appear to have been previously examined. The conclusions drawn for these earlier studies would also appear to be in doubt as glass substrates were used which possibly contained Fe impurities and anyway the films were usually incompletely oxidised making analysis difficult. The work reported here appears to be the first detailed and extensive study of passive film structure using EXAFS.

The structure of the passive film on iron has been determined from the *in-situ* measurements, and it would seem to be best described as a disordered $\gamma-FeOOH$-like structure but with little long range order. This conclusion is consistent with that first suggested by O'Grady[31], on the basis of Mössbauer results (Fig. 6.1). The results presented here represent, however, the first direct *in-situ* structural confirmation of this suggestion. Although the incorporation of other species such as Cr and B, from either the electrolyte solution or

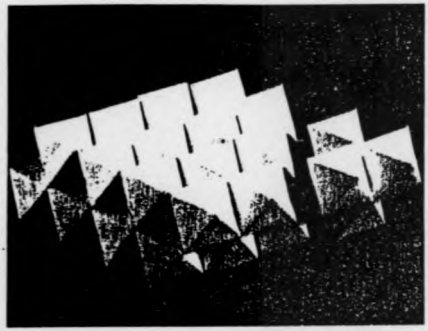

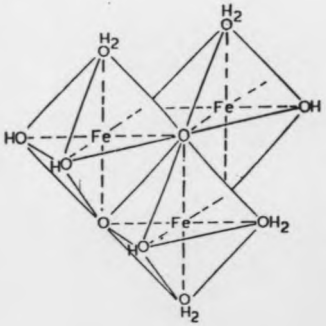

Fig. 6. 1. A representation of the structure of the passive film and the basic building unit, trimers of $[FeO_6]$ octahedra[31].

the alloy, lead to an increase in the radius of the second shell, there are no other detectable changes in the structure, even for Fe/Cr alloys. The only significant structural changes with alloy composition are seen in the case of samples passivated in an electrolyte which does not incorporate any species. In this case there appears to be a small increase in the disorder with increasing Cr content.

In the past there has been much discussion of whether structures determined *ex-situ* are the same as the *in-situ* ones and possible restructuring has been one of the main criticisms of the electron diffraction studies of passive films. One of the great advantages of the EXAFS technique is that it can be applied both *in-situ* and *ex-situ*. In the present case the structure, as determined by EXAFS, was found to be insensitive to drying, always being 'γ−FeOOH like'. *Ex-situ* electron diffraction results on the other hand essentially suggest that the passive film has the structure of γ−Fe_2O_3 [4−6]; though it is sometimes suggested that this has arisen from the transformation of γ−FeOOH. It is always possible to transform γ−FeOOH to γ−Fe_2O_3 but this requires high energies (i. e. at elevated temperatures) and is not expected to occur on simple drying. It is however possible that it can take place when the sample is exposed to an electron beam which can cause local heating. This may explain the difference between the electron diffraction and EXAFS work. The results presented here however show that it is no longer necessary to rely on the *ex-situ* investigations to determine the structure of thin surface films but that *in-situ* ones are now possible. Based on *ex-situ* electron diffraction results Kuroda *et al*[6] have suggested that the passive film formed on Fe in Fe^{2+} free electrolyte is γ−Fe_2O_3 but in the presence of Fe^{2+} γ−FeOOH film is found. Interestingly on the basis of the *in-situ* EXAFS study reported here it would seem that in the presence, or absence, of Fe^{2+} the same structure is observed.

It is of course well known that the addition of Cr to Fe leads to an improvement in the corrosion resistance of the alloy. On the basis of the Fe K-edge EXAFS studies the only effect

of the addition of Cr seems to be the lengthening of the radius of second shell (i.e. of the first Fe-Fe distance). This on its own cannot explain the improved corrosion resistance. It is indeed the presence of Cr in the film that appears to be responsible for it. The photocurrent spectroscopy results suggested that for high Cr content alloys the passive film was very thin as the photocurrents were very small. Additionally they showed that there appeared to be two phases present, the relative amounts being dependent on the formation potential of the film. At low potentials the film appeared to contain mainly chromium and little of any oxidised iron. In the past the chromium phase has been referred to as Cr_2O_3 or hydrated Cr_2O_3. The EXAFS results presented in this work indicate clearly that the structure of the Cr containing part of the passive layer is similar to that of the amorphous $Cr(OH)_3$ compound and certainly not to that of Cr_2O_3. Additionally the structure of this phase seemed to be unaffected by the presence of any other species.

By combining the XANES and EXAFS results at the Fe and Cr K-absorption edges the structure of the passive film formed, either by simple immersion or electrochemically, on Fe/Cr alloys is therefore best described as a mixture of two disordered γ-FeOOH-like and $Cr(OH)_3$ phases. The $Cr(OH)_3$ like phase being a particularly efficient passivator. In the case of Fe passivated in potassium chromate solution the $Cr(OH)_3$ phase found within the passive film was probably obtained by precipitation after the chromate ions have oxidised iron from Fe to Fe^{3+} and therefore chromium was reduced from Cr^{6+} to Cr^{3+}. This may be illustrated by the following equilibrium

$$CrO_4^{2-} + Fe + 3H_2O \rightleftharpoons Cr(OH)_3 + FeOOH + 2OH^-$$

The electrochemical passivation of pure iron as a function of the anodic potential has shown no changes in the structure of the passive film. However, future EXAFS studies at Fe and Cr K-absorption edges on Fe/Cr alloys in this way are needed. This may lead to interesting conclusions since the photocurrent spectroscopy data derived for the Fe15%Cr

alloy has shown a change in the effective optical band gap energy of the passive film as the anodic potential at which it is formed varies. It is thought that this arises from variation of relative amounts of the Fe and Cr containing 'oxides' on the surface and it should be possible to test this hypothesis using EXAFS.

Although the EXAFS analysis by using EXCURVE[56] program provides a good approach to modelling structures, it was not possible to analyse mixed phases containing the same absorbing atom. However, it is hoped that further light will be thrown on the structure determination of the passive film on pure iron in the presence of a detectable amount of the metallic phase. In the work presented in this thesis incomplete oxidation of the sample frequently occurred. This did not significantly hinder the analysis of the first shell (Fe-O or Cr-O) and identical conclusions were reached as for completely oxidised samples. Fitting the second shell for incompletely oxidised samples was always rather difficult however because of the contribution from the first shell of the unoxidised metal which was at a similar radius. It would be interesting to analyse such data by subtracting EXAFS of the metallic phase bearing in mind the different absorption cross-sections. The procedure would have to be repeated several times with various amounts of the metallic phase till the absorption spectrum is free from the metallic iron contribution.

The work described in this thesis was concerned with a limited range of electrolytes. In the future it could be extended by including the *in-situ* EXAFS investigations of the passive film formed electrochemically in other solutions such as sulphuric acid and sulphate solutions. Perhaps a good comparison to the results presented here are those which may be obtained *in-situ* by using REFLEXAFS. This mode has a great advantage in performing experiments on bulk material even though it is extremely difficult to use as the experiment requires very smooth flat surfaces. The alignment of the X-rays beam is also a big problem as is electrolyte penetration.

One of the major problems with iron and its alloys in corrosion is the localised corrosion. The products of this type of corrosion have only been studied by using spectroscopic techniques *ex-situ*. It would be interesting to develop micro-focused beams enabling one to look into pits *in-situ* and record the EXAFS.

For many years, there has been controversy between two thoughts about explaining how the corrosion of iron is inhibited when a substance is added to a corrosive solution. One is that by the adsorption of molecules of the inhibitor and the other is that the inhibition is attributed to a protective film formed by reaction between metal and the inhibitor. Research in this area by using EXAFS techniques will certainly throw some light on the description of inhibition caused by the addition of different substances, both organic and inorganic, into solutions.

The techniques outlined here can also be used to study other systems such as sulphides and phosphates. For instance, the presence of copper in steel increases considerably its corrosion resistance which is believed to be due to the formation of a stable copper sulphide compound.

The work presented here has been successfully completed and the main objectives realised are the structural determination of the passive film on iron from *in-situ* measurements and the identification of the mechanism by which chromium improves the corrosion resistance. The structure obtained for the passive film is best described as a disordered $\gamma-FeOOH$ and was found to be insensitive to drying. The structure of the chromium containing phase in the passive film on Fe/Cr alloys and in that on Fe dipped in chromate solution has not previously been identified and was referred to as Cr_2O_3, or hydrated Cr_2O_3, phase. As a result of these studies the structure of this phase is now firmly established and found to have a $Cr(OH)_3$-like structure.

References

1. U.R. Evans, *An Introduction to Metallic Corrosion*, 3rd edition (1981) 248

2. M. Cohen, in *Passivity of Metals*, R.P. Frankental (1978) 521

3. R. Olivier, in *Passiviteit Van Ijzer en Ijzer-Chroom Legeringen*, Dissertation Leiden (1955); Proc. Sixth Meeting CITCE, Butterworths Scientific Publications, London, (1954) 314

4. M. Nagayama and M. Cohen, J. Electrochem. Soc., **109** (1962) 781

5. C.L. Foley, J. Kruger and C.J. Bechtold, J. Electrochem. Soc., **126** (1979) 442

6. K. Kuroda, B.D. Cahan, Gh. Nasri, E. Yeager and T.E. Mitchell, J. Electrochem. Soc., **129** (1982) 2163

7. M.E. Brett, K.M. Parkin and M.J. Graham, J. Electrochem. Soc., **133** (1986) 2031

8. H. Konno and M. Nagayama in *The Corrosion and Oxidation of Metals*, U.R. Evans, (1968) 585

9. G.G. Long, J. Kruger, D.R. Black and M. Kuriyama, J. Electrochem. Soc., **130** (1983) 240

10. G.G. Long, J. Kruger, M. Kuriyama, D.R. Black, E.N. Farabaugh, D.M. Sanders and A.I. Goldman, Proc. Int. Congr. Met. Corros. NRCC: Ottawa, Ont., (1984) 419

11. J. Kruger, G.G. Long, M. Kuriyama and A.I. Goldman, in *Passivity of Metals*, R.P. Frankenthal, (1978) 163

12. Z. Syklarska and W. Kozlowski, in *Passivity of Metals and Semiconductors*, M. Froment, (1983) 89

13. J.L. Ord, in *Passivity of Metals and Semiconductors*, M. Froment, (1983) 95

14. C.C. Chen and B.D. Cahan, J. Electrochem. Soc. **129** (1982) 18

15. Z.Q. Huang and J.L. Ord, J. Electrochem. Soc., **132** (1985) 24

16. J. Donnwald, R. Lossy and A. Otto, in *Passivity of Metals and Semiconductors*, M. Froment, (1983) 107

17. M. Froelicher, A. Hugot-Le Goff, C. Pallotta, R. Dupeyart and M. Masson, in *Passivity of Metals and Semiconductors*, M. Froment, (1983) 101

18. A. Hugot-Le Goff and C. Pallotta, J. Electrochem. Soc., Accelerated Brief Communication, (1985) 2806

19. I.C.G. Thanos, J. Electroanal. Chem., 210 (1986) 259

20. L.M. Abrantes and L.M. Peter, J. Electroanal. Chem., 150 (1983) 593

21. C.T. Chen and B.D. Cahan, J. Electrochem. Soc., 129 (1982) 17

22. C. Sunseri, S. Piazza, A. Di Paola and F. Di Quarto, J. Electrochem. Soc., 134 (1987) 2410

23. M. Froelicher, A. Hugot-Le Goff and V. Javancicevic, in *Passivity of Metals and Semiconductors*, M. Froment, (1983) 491

24. U. Stimming, in *Passivity of Metals and Semiconductors*, M. Froment, (1983) 477

25. P.C. Searson, R.M. Latanision and U. Stimming, J. Electrochem. Soc., 135 (1988) 1358

26. S.M. Wilhelm, K.S. Yun, L.W. Ballenger and N. Hackerman, J. Electrochem. Soc., 126 (1979) 419

27. S.M. Wilhelm and N. Hackerman, J. Electrochem. Soc., 128 (1981) 1668

28. J.S. Curran and W. Gissler, J. Electrochem. Soc., 126 (1979) 56

29. R.M. Candea, Electrochimica Acta, 26 (1981) 1803

30. R. Peat and L.M. Peter, J. Electroanal. Chem., 228 (1987) 351

31. W. O'Grady, J. Electrochem. Soc., 127 (1980) 555

32. M.E. Kordesch and R.W. Hoffman, Nucl. Instr. and Meth., 222 (1984) 347

33. J.M. Fine, J.J. Rusek, J. Eldrige, M.E. Kordesch, J.A. Mann, R.W. Hoffman and D.R. Sandstrom, J. Vac. Sci. Technol. A 1(2), (1983) 1036

34. K.J. Vetter, *Electrochemical Kinetics*, Academic Press, New York (1967)

35. C. Wagner, Ber. Bunsenges. Phys. Chem., 77 (1973) 1090

36. H.H. Uhlig, Acta. Metall., 4 (1956) 541

37. M. Nagayama and M. Cohen, J. Electrochem. Soc., 110 (1963) 670

38. J.W. Shultze, in *Passivity of Metals*, R.P. Frankenthal and J. Kruger, Editors, The Electrochemical Society, Princeton, NJ (1978)

39. K. Kudo, T. Shibata, G. Okamoto and N. Sato, Corros. Sci., 8 (1968) 809

40. E.K. Oshe and I.L. Rosenfel'd, Electrokhimiya, 4 (1968) 1200

41. W.W. Gaertner, Phys. Rev., 116 (1959) 84

42. M.A. Butler, J. Appl. Phys., 48 (1977) 1914

43. U. Stimming, Electrochemica Acta, 31 (1986) 415

44. K. Leitner, J.W. Shultze and U. Stimming, J. Electrochem. Soc., 133 (1986) 1561

45. F. Moellers, H.J. Tolle and R. Memming, J. Electrochem. Soc., 121 (1974) 1160

46. R.H. Bube, *Photoconductivity of Solids*, Wiley, New York (1967)

47. J.I. Paukove, *Optical Processes in Semiconductors*, Dover, New York (1975)

48. D.E. Sayers, E.A. Stern and F.W. Lytle, Phys. Rev. Lett., 27 (1971) 1204

49. P.A. Lee and J.B. Pendry, Phys. Rev. B, 11 (1975) 2795

50. G. Beni and P.H. Platzmann, Phys. Rev. B, 14 (1976) 9514

51. J. M. Taylor, Ph.D. Thesis, University of Warwick, U.K. (1984)

52. P.A. Lee and G. Beni, Phys. Rev. B, 11 (1977) 2795

53. P.A. Lee and G. Beni, Phys. Rev. B, 15 (1977) 2862

54. B.K. Teo and P.A. Lee, J. Amer. Chem. Soc., 101 (1979) 2815

55. S.J. Gurman and J.B. Pendry, Solid State Comm., 30 (1976) 287

56. S.J. Gurman, N. Binstead and I. Ross, J. Phys. C: Solid State Phys., 17 (1984) 143

57. E. Pantos and G.D. Firth, *The EXAFS Data Base: Proposed Specification*, Daresbury Laboratory Technical Memorandum, DL/CSE/TM21, October (1982)

58. B. Kincaid, Ph.D. Thesis, Stanford University, USA (1976)

59. S.S. Hasnain, P.D. Quinn, G.P. Diakun, E.M. Wardell and C.D. Garner, J. Phys. E: Sci. Instr., **17** (1984) 11

60. M.J. Van Der Hoek, W. Werner, P. Van Zuylen, B.R. Dobson, S.S. Hasnain, J.S. Worgan and G. Luijckx, Nuclear Instruments and Methods in Physics Research, **246** (1986) 380 (North-Holland, Amsterdam)

61. J. Jaklevic, J.A. Kirby, M.P. Klein, A.S. Robertson, G.S. Brown and P. Eisenberger, Sol. State Commun., **23** (1977) 679

62. R.G. Shulman, P. Eisenberger, B.K. Teo, B.M. Kincaid and G.S. Brown, J. Mol. Biol., **124** (1978) 305

63. S.P. Cramer, O. Tench and G.N. George, Schlumberger-Doll Research, EMG (1987) 47

64. C.L. Foley, J. Kruger and C.J. Bechtoldt, J. Electrochem. Soc., **114** (1967) 994

65. A.G. Revesz and J. Kruger, in *Passivity of Metals*, R.P. Frankenthal and J. Kruger, The Electrochemical Society, Princeton, (1978) 137

66. V. Markovac and M. Cohen, J. Electrochem. Soc., **114** (1967) 678

67. J.L. Leibenguth and M. Cohen, J. Electrochem. Soc., **119** (1972) 987

68. R.F. Pettifer, Ph.D. Thesis, Warwick University, U.K. (1978)

69. G. Okamoto, Tokyo Cong., (1972), Plenary Lecture and in *The Corrosion and Oxidation of Metals*, U.R. Evans, (1976) 146

70. P.C. Searson, R.M. Latanision and U. Stimming, J. Electrochem. Soc., **135** (1988) 1358

71. A. Szytula, A. Burewics, Z. Dimitrijewic, S. Krasnicki, H. Rzany, J. Todorovic, A. Wanic and W. Wolski, Physica Status Solidi, **26** (1968) 429

72. A.N. Christensen, P. Hansen and M.S. Lehmann, Journal of Solid State Chemistry, **21** (1977) 325

73. S. Chung, J. Robinson and G.E. Thompson, to be published